Title
Time Resolved Structural Studies of Photochemical Processes Using Resonance Raman

Author
Creelman, Mark Ryan

Publication Date
2013

Peer reviewed|Thesis/dissertation

Time Resolved Structural Studies of Photochemical Processes Using Resonance Raman

By

Mark Ryan Creelman

A dissertation submitted in partial satisfaction of the

requirements for the degree of

Doctor of Philosophy

in

Chemistry

in the

Graduate Division

of the

University of California, Berkeley

Committee in charge:

Professor Richard A. Mathies, Chair
Professor Graham R. Fleming
Professor Joseph Orenstein

Fall 2013

Time Resolved Structural Studies of Photochemical Processes Using Resonance Raman

by Mark Ryan Creelman

Abstract

Time Resolved Structural Studies of Photochemical Processes Using Resonance Raman

By

Mark Ryan Creelman

Doctor of Philosophy in Chemistry

University of California, Berkeley

Professor Richard A. Mathies, Chair

I have used femtosecond time resolved resonance Raman spectroscopy to probe vibrational dynamics during ultrafast photochemical reactions in synthetic and biological materials, revealing nuclear motions that play key roles in the photoactivity of these systems. These results expose mechanistically significant structural details important for advancing our fundamental understanding of photochemical processes and our ability to design improved photoactive materials. In performing these studies I have improved the capabilities of tunable femtosecond stimulated Raman spectroscopy (FSRS) by developing high-throughput detection techniques and by redesigning the optical layout of the instrument for improved performance, tune-ability, and time-resolution.

My initial studies were performed on a synthetic photoactive system relevant for electron transfer. The iron(II) complex, $[Fe(tren(py)_3)]^{2+}$, is a spin-crossover compound that undergoes an ultrafast $\Delta S = 2$ transition upon excitation of its metal-to-ligand charge transfer band at ~ 560 nm. Using time resolved FSRS I was able to record the vibrational dynamics of this intersystem crossing during the 5 ps following actinic initiation of the photochemistry. Analysis of the time resolved vibrational spectra show that the spin-crossover process takes place in < 200 fs, and is intimately associated with the expansion of iron-ligand bonds, providing important temporal and structural characterization of the photoreactivity of this compound.

I have also completed a study of the structural dynamics of the biological photoreceptor photoactive yellow protein (PYP). Upon absorption of light, the PYP chromophore, *para*-hydroxy-cinnamic acid, undergoes *trans-cis* isomerization in < 3 ps defining the primary photochemistry of the PYP photocycle. The constraints on the chromophore imposed by the protein binding pocket suggest an isomerization mechanism that involves the out-of-plane rotation of the chromophore's C_9=O carbonyl. Using FSRS I was able to acquire vibrational spectra of the PYP chromophore from 0 fs to 300 ps following photoexcitation, recording the dynamics of the C_9=O out-of-plane vibration during the initiation of the PYP photocycle for the first time. Following excitation, these data show structural evidence for a ~ 150 fs charge shift in the chromophore excited state preceding isomerization. The frequency of the C_9=O out of plane vibration downshifts in ~ 800 fs as the excited chromophore decays to the early cissoid photocycle intermediate, I_0, confirming the key role of carbonyl motion for entering the active photocycle. Following formation of I_0, the structure of the chromophore is highly distorted. The

relaxation of this distortion is likely a key driving force for the continuation of the PYP photocycle.

The results presented in this work provide important benchmarks for the two systems studied, as well as laying the groundwork for future mechanistic studies on a variety of photochemical systems. The technique and methodology presented may be applied to the development of synthetic photoactive materials in a straightforward way, providing chemists with a direct means of identifying structural elements that promote the desired photoactivity. These experiments demonstrate the value of time resolved structural characterization in developing a clear understanding of ultrafast chemical processes, in addition to demonstrating FSRS' potential as a valuable tool for revealing the relationship between structure and function in photochemical systems.

To

Mom, Papa, and Eric

Table of Contents

List of Figures

Acknowledgement

Having been lucky enough to tenure a fairly lengthy graduate school career, I have had the pleasure of making the acquaintance of many talented colleagues who have provided guidance, assistance, and moral support to me in my scientific endeavors, and without whom this work would not be possible.

First, I thank my scientific mentor, Professor Richard Mathies, for guiding me through my research, and instilling in me not only a methodology for tackling scientific problems, but a philosophy as well. He has taught me nearly all I know about scientific writing, and how to compose my research with "high signal to noise." Most importantly he has taught me to savor the moments when science surprises you, and relish the opportunity for new discovery. The skills I have acquired through my work in Rich's group will continue to serve me for the rest of my life.

I would also like to thank Mary, who kept Rich's lab running for most of my graduate school career, and Dennie, who currently keeps the lab running. Mary and Dennie have both been invaluable resources to me throughout my time at Berkeley; words cannot express my gratitude.

I additionally must thank my former and current lab-mates, we've shared some laughs, some sighs, and a few cries, and I couldn't have done it without them. I thank Renee who taught me my way around a laser table, and who was instrumental in helping me perform my early FSRS experiments. Chris and Rosalie taught me everything I know about taking spontaneous Raman spectra. Jyotishman is a scientific inspiration, and has, with unmatched enthusiasm, provided me with many helpful discussions. Ryan is a MacGyver in the lab and his love of gadgetry has spawned a series of valuable lab DIY projects in the Mathies group. David H. has contributed innumerable advances to FSRS, from data analysis to instrumentation, and has provided me with many crucial insights over the years. Amy is the most talented chemist in the Mathies group, and has provided much helpful advice as well as helping me maintain my sanity through the thesis writing process.

Finally I thank my mother, father, and brother, who have been waiting for me to finish graduate school in "a couple of years" for the last five years. Their love, patience, and support saw me through the ups and downs of graduate school, and have truly made this work possible.

Chapter 1

Introduction

1.1 Motivation

The influence of light on chemistry has shaped nearly every facet of the natural world. Indeed, life itself would not exist were it not for the influx of electromagnetic radiation from the Sun. The intimate relationship between life and light is made readily apparent by the diverse evolution of organisms with specialized systems for sensing, harnessing, reacting to, and protecting against it. These various tasks are made possible by specialized proteins capable of converting photons to chemical energy, which is subsequently used to trigger a biological response. Such photoactive proteins consist of specialized chromophores that undergo highly specific and evolutionarily tuned structural changes upon absorption of a photon. The capture and direction of light energy also has many useful technological applications that motivate the development of synthetic photoactive materials. These applications vary widely, from the photolithographic polymers used to manufacture our ever-shrinking electronic devices, to materials that harness the Sun's energy to power them. As in biology, the development of such technology requires the ability to tailor photoactive molecules to perform specific chemistry upon the absorption of light.

The ubiquity of photoactivity in biology and artificial materials and devices necessitates a thorough understanding of the chemistry that occurs in these systems following light activation, both to develop a fundamental understanding of our physical world and to advance current technology. Ultimately, it is desirable to identify the key structural features and nuclear motions that promote the photochemistry of interest, along with those of competing processes in order to develop a clear picture of the structure/function relationships that drive photochemical processes. Such knowledge will lead to the development of improved photoactive materials, as well as an increased understanding of the complex photoactivity in biology.

In this endeavor it is necessary to be able to track nuclear motion on the timescale of femtoseconds to picoseconds as the molecule evolves. To this end, femtosecond stimulated Raman spectroscopy (FSRS) is the ideal experimental technique because of its ability to measure vibrational spectra on these timescales with excellent energy resolution.[1,2] Additionally, FSRS is ideally suited to making measurements in the solution phase at physiological temperatures relevant to the native environment of biomolecules. Furthermore, as a Raman technique, it is possible to selectively enhance the signals from specific chromophores within large protein structures, as well as from different transient electronic states.

In this thesis FSRS is used to reveal key photoinduced structural dynamics relating to photoproduct formation in an iron(II) based solar energy conversion model system and an important biological photoreceptor, photoactive yellow protein.

1.2 $[Fe(tren(py)_3]^{2+}$: a Prototype Sensitizer Dye

Iron(II) complexes, such as $[Fe(tren(py)_3]^{2+}$, undergo rapid conversion from a low-spin state to a high-spin state upon photoexcitation (**Figure 1.1**). This low- to high-spin conversion is accompanied by dramatic changes in the absorption, magnetic and structural properties of the compound.[3] Due to their interesting photochemical and photophysical properties, in addition to the low cost and abundance of iron, iron(II) complexes have a number of potentially useful applications.

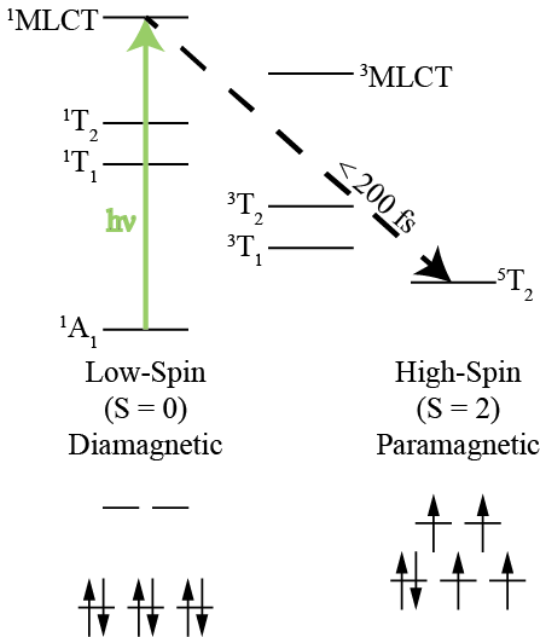

Figure 1.1 Absorption of light by iron(II) complexes triggers ultrafast spin crossover.

$[Fe(tren(py)_3]^{2+}$ was chosen for study primarily because it is a prototype of low cost iron dyes for use in dye sensitized solar cells (DSSCs)[4,5] though it also of interest as a magneto-optical material.[6] An illustration of a DSSC is shown in **Figure 1.2**. Strongly absorbing dye molecules are adsorbed onto the surface of nanoparticulate TiO_2. Absorption of a photon by the dye results in transfer of the excited electron from the dye to the conduction band of TiO_2. The electrons are subsequently transferred through a nanocrystalline film of sensitized TiO_2 to the working electrode of the solar device, while an electrolytic solution restores the electron to the dye.[7] Such cells are much easier to fabricate than silicon based devices. Unfortunately, to date the most efficient sensitizer dyes known are ruthenium based, limiting their affordability and scalability. Iron, on the other hand, is orders of magnitude more abundant and affordable than ruthenium, thus the development of feasible iron based dyes would significantly lower the cost of DSSCs making them economically viable. However, the efficiency of devices made with current iron(II) dyes is too low. This low efficiency is attributed to the rapid formation of the high-spin quintet state following photoexcitation, which does not efficiently transfer an electron to the TiO_2 conduction band.

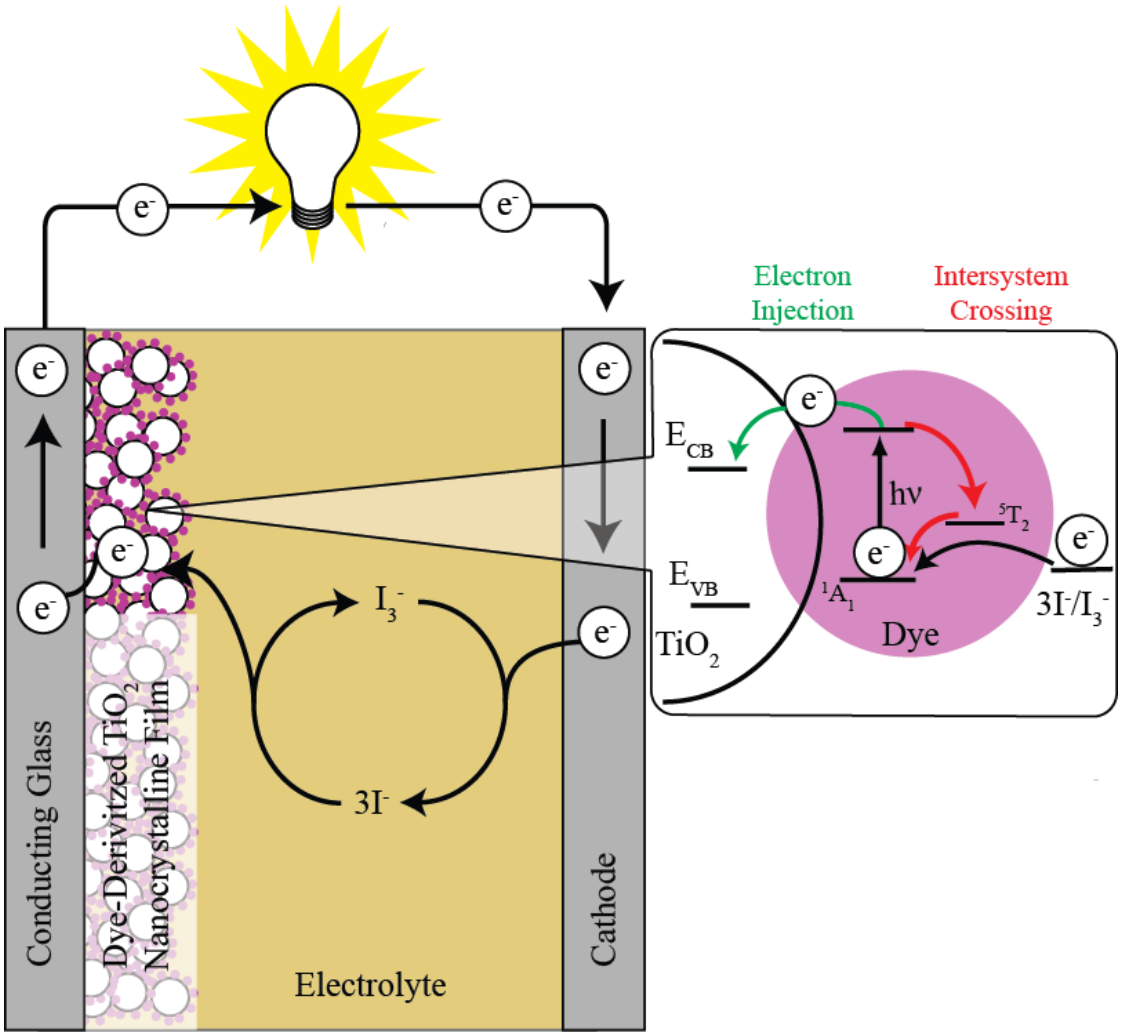

Figure 1.2 Illustration of a dye sensitized solar cell showing the flow of electrons initiated by absorption of a photon. E_{CB} and E_{VB} represent the conduction and valence bands of TiO_2, respectively. Exciting the dye can result in the desired electron injection pathway (green) or the competing intersystem crossing pathway (red) resulting in quintet formation in the case of $[Fe(tren(py)_3]^{2+}$.

By studying the structural dynamics of this iron(II) dye in solution we hope to identify the key nuclear dynamics accompanying the quintet formation. Once the structural changes leading to the high-spin state have been identified, is it possible to formulate synthetic design strategies to limit or enhance this pathway, as the desired application dictates? Synthetic chemists are only able to control the structures of the molecules they design, so it is crucial to understand, and be able to analyze, which structural elements bring about the desired functionality.

1.3 Photoactive Yellow Protein: a Bacterial Photoreceptor

Photoactive yellow protein (PYP) is a small photoreceptor protein responsible for blue light avoidance in certain species of phototropic halophilic bacteria. Absorbance of blue light by PYP causes *trans-cis* photoisomerization of its covalently bound *p*-hydroxy-cinnamic acid chromophore (**Figure 1.3**). This isomerization, which is complete in a few picoseconds, is the first step in a photocycle that actuates partial, temporary unfolding of the protein before returning to the dark state. This complex photocycle involves evolutions through several intermediates on time scales ranging from femtoseconds to milliseconds.[8,9]

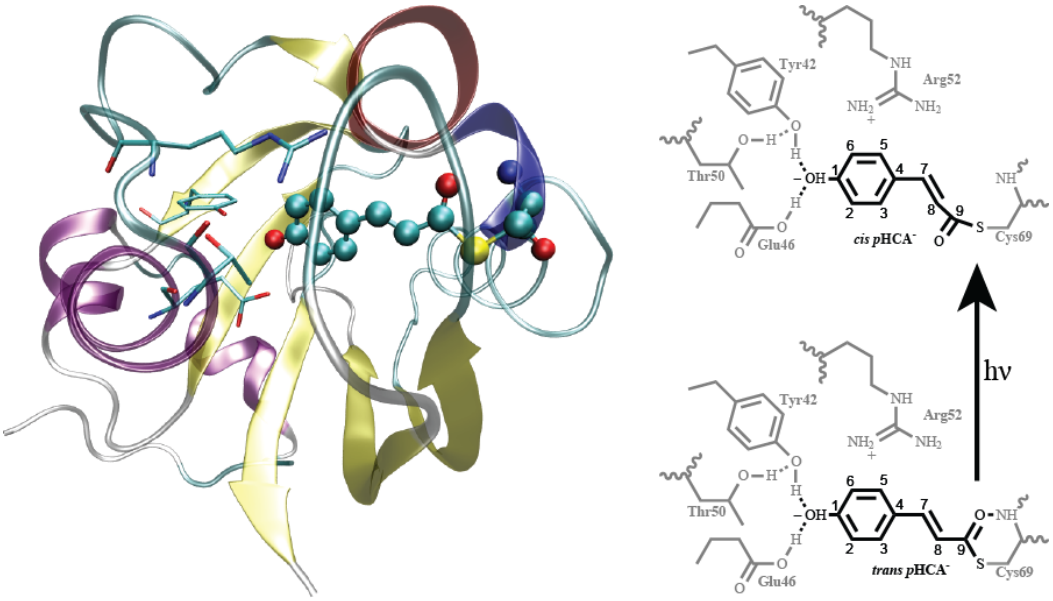

Figure 1.3 Photoactive yellow protein. Left: The global structure of PYP. The *para*-hydroxy-cinnamic acid chromophore is represented in ball and stick form, the chromophore pocket side chains appear as tubes, and the protein backbone is displayed in ribbon form. Right: Photoexcitation results in *tran-cis* isomerization about the chromophore's C_7=C_8 bond.

While the PYP photocycle has been extensively studied, a complete understanding of the structural dynamics during the initial photoisomerization is lacking. Previous studies have concluded that during the *trans-cis* isomerization the phenolate end of $pHCA^-$ remains essentially stationary. This has lead to the conclusion that isomerization must occur through the out of plane rotation of the C_9=O carbonyl, and breaking of the hydrogen bond with Cys69. While there is strong experimental evidence showing weakening of the hydrogen bond, and the formation of *cis* isomerized chromophore, little is known about the nuclear motions that occur during the isomerization. While time resolved vibrational spectra have been reported,[10–13] the spectral windows were limited and omitted the important low frequency modes including the C_9=O out of plane vibration at 644 cm^{-1} and vibrations of the ethylenic tail. In order to make assertions about the reaction mechanism, as well as identifying other potentially relevant nuclear motions leading to chromophore isomerization, it is important to be able to monitor these reactive motions.

Using time resolved FSRS it was possible to acquire vibrational spectra of the PYP chromophore from 200 to 1800 cm^{-1} as it evolved from the initially populated Franck-Condon (FC) region to the cissoid photoproduct, I_0, during the early stages of the PYP photocycle. In order to selectively enhance signals from the PYP chromophore, the FSRS experiments were carried out with visible Raman excitation, requiring further development of the tunable FSRS system. Even with resonance enhancement vast improvement of the detection system was required to collect data of sufficient signal to noise from the weakly scattering chromophore. This and many other design changes I made to the tunable FSRS system, which will be detailed in the next chapter, have culminated in a user-friendly and versatile instrument capable of rapidly acquiring high quality data.

1.4 Outline

A discussion of the FSRS technique and instrumentation used in these studies is presented in Chapter 2. The chapter begins with an introduction to FSRS, including a discussion of the theory and capabilities. The tunable FSRS instrument I developed for these studies is presented including a detailed description of the laser and detection systems. Sample handling, experimental considerations, and potential design improvements are also discussed.

The application of time resolved FSRS to the inorganic charge transfer complex, $Fe(tren(py)_3)^{2+}$, is presented in Chapter 3. Vibrational spectra of the system from 0 fs to 6 ps were acquired as it underwent conversion from low to high spin. The structural dynamics of this complex were analyzed along side transient absorption data revealing the expansion of the metal-ligand bonds during the 200 fs formation of the quintet state and fully characterizing the timescale of this reaction for the first time. This study established FSRS as a powerful tool in the analysis of synthetic photoactive materials.

In Chapter 4 FSRS studies on the chromophore dynamics during the first 300 ps of the PYP photocycle are presented. Tunable FSRS was used to observe the complex vibrational dynamics of the PYP chromophore as it transitioned from its FC structure to early isomerized photocycle intermediates. The large FSRS spectral window (200-1800 cm^{-1}) made it possible to record the dynamics of low frequency vibrations not included in prior transient vibrational spectroscopy of PYP. The kinetics of the transient Raman modes are analyzed and discussed, indicating the timescales of key structural dynamics and features of the intermediates. Observation of the C_9=O vibration provided direct structural evidence supporting the carbonyl out of plane rotation mechanism. In addition to corroborating this hypothesis, the study provides new structural evidence for excited state charge shift upon photoexcitation, and reveals the time ordering of important structural transitions leading to and following photoisomerization. This study also demonstrates the utility of tunable FSRS for studying proteins with small, weakly scattering chromophores, such as the xanthopsins.

Finally, the conclusions and implications of this thesis are summarized in Chapter 5, along with a discussion of future studies and advances in the FSRS technique.

1.5 References

(1) Kukura, P.; McCamant, D. W.; Mathies, R. A. Femtosecond Stimulated Raman Spectroscopy. *Annu. Rev. Phys. Chem.* **2007**, *58*, 461–488.

(2) Frontiera, R. R.; Mathies, R. A. Femtosecond Stimulated Raman Spectroscopy. *Laser Photonics Rev.* **2011**, *5*, 102–113.

(3) Gütlich, P.; Goodwin, H. A. Spin Crossover—An Overall Perspective. In *Spin Crossover in Transition Metal Compounds I*; Gütlich, P.; Goodwin, H. A., Eds.; Topics in Current Chemistry; Springer Berlin Heidelberg, **2004**; pp. 1–47.

(4) Monat, J. E.; McCusker, J. K. Femtosecond Excited-State Dynamics of an Iron(II) Polypyridyl Solar Cell Sensitizer Model. *J. Am. Chem. Soc.* **2000**, *122*, 4092–4097.

(5) Ferrere, S.; Gregg, B. A. Photosensitization of TiO2 by $[Fe^{II}$(2,2‘-Bipyridine-4,4‘-Dicarboxylic acid)$_2(CN)_2]$: Band Selective Electron Injection from Ultra-Short-Lived Excited States. *J. Am. Chem. Soc.* **1998**, *120*, 843–844.

(6) Létard, J.-F. Photomagnetism of iron(II) Spin Crossover Complexes—the T(LIESST) Approach. *J. Mater. Chem.* **2006**, *16*, 2550–2559.

(7) Grätzel, M. Dye-Sensitized Solar Cells. *J. Photochem. Photobiol. C Photochem. Rev.* **2003**, *4*, 145–153.

(8) Hellingwerf, K. J.; Hendriks, J.; Gensch, T. Photoactive Yellow Protein, A New Type of Photoreceptor Protein: Will This “Yellow Lab” Bring Us Where We Want to Go? *J. Phys. Chem. A* **2003**, *107*, 1082–1094.

(9) Larsen, D. S.; van Grondelle, R.; Hellingwerf, K. J. Primary Photochemistry in the Photoactive Yellow Protein: The Prototype Xanthopsin. In *Ultrashort Laser Pulses in Biology and Medicine*; Biological And Medical Physics Biomedical Engineering; Springer Berlin Heidelberg, **2008**; pp. 165–199.

(10) Groot, M. L.; van Wilderen, L. J. G. W.; Larsen, D. S.; van der Horst, M. A.; van Stokkum, I. H. M.; Hellingwerf, K. J.; van Grondelle, R. Initial Steps of Signal Generation in Photoactive Yellow Protein Revealed with Femtosecond Mid-Infrared Spectroscopy. *Biochemistry.* **2003**, *42*, 10054–10059.

(11) Van Wilderen, L. J. G. W.; van der Horst, M. A.; van Stokkum, I. H. M.; Hellingwerf, K. J.; van Grondelle, R.; Groot, M. L. Ultrafast Infrared Spectroscopy Reveals a Key Step for Successful Entry into the Photocycle for Photoactive Yellow Protein. *Proc. Natl. Acad. Sci. U. S. A.* **2006**, *103*, 15050–15055.

(12) Heyne, K.; Mohammed, O. F.; Usman, A.; Dreyer, J.; Nibbering, E. T. J.; Cusanovich, M. A. Structural Evolution of the Chromophore in the Primary Stages of Trans/Cis Isomerization in Photoactive Yellow Protein. *J. Am. Chem. Soc.* **2005**, *127*, 18100–18106.

(13) Nakamura, R.; Hamada, N.; Abe, K.; Yoshizawa, M. Ultrafast Hydrogen-Bonding Dynamics in the Electronic Excited State of Photoactive Yellow Protein Revealed by Femtosecond Stimulated Raman Spectroscopy. *J. Phys. Chem. B* **2012**, *116*, 14768–14775.

Chapter 2

Apparatus and Methods

2.1 Femtosecond Stimulated Raman Spectroscopy

Femtosecond stimulated Raman spectroscopy (FSRS) is an ultrafast, time-resolved technique capable of probing structural details of reacting photochemical systems with high temporal (~ 50 fs) and vibrational (~ 10 cm^{-1}) resolution. To perform time-resolved FSRS a short (~ 30 fs) visible actinic pulse excites a ground state population onto a reactive potential energy surface with high time precision. Following actinic initiation, the stimulated Raman spectrum is acquired at various time delays to produce a series of time resolved vibrational spectra of the reacting system as it evolves along the excited state and photoproduct potential energy surfaces (**Figure 2.1**).[1–3]

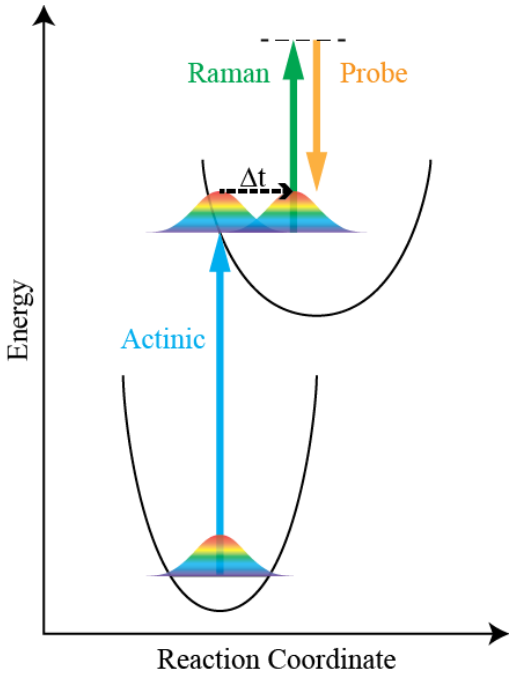

Figure 2.1 Diagram of the time resolved FSRS experiment. The actinic pulse (cyan) promotes a ground state population to the excited state potential energy surface, where it is allowed to evolve for time Δt before the Raman (green) and probe (orange) pulses acquire the stimulated Raman spectrum.

Stimulated Raman spectra are acquired using a narrowband, picosecond Raman pulse (typically ~ 0.6-4 ps, ~ 20-4 cm^{-1}, ~ 0.2-4 μJ) in combination with a weak femtosecond probe pulse (typically < 20 fs, ~ 2000 cm^{-1}, ~ 5 nJ). The Raman pulse provides a well-defined virtual state in the Raman process and the broadband probe pulse simultaneously stimulates Raman transitions across a large spectral region, producing sharp gain features on top of the probe pulse envelope (**Figure 2.2**). The natural logarithm of the quotient of this sharp-featured pump-on probe spectrum by the smooth pump-off probe spectrum acquired without the Raman pulse produces a normalized Raman gain spectrum (**Figure 2.2, inset**). The probe pulse is typically tuned to the red of the Raman pulse to stimulate Stokes transitions, and the polarization of these two pulses is matched to produce parallel-polarized Raman spectra.

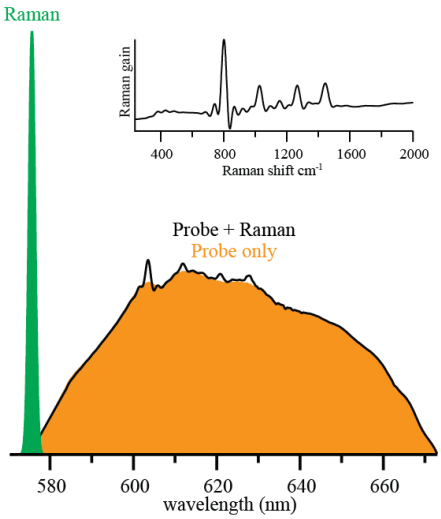

Figure 2.2 The Raman (green) and probe (orange) pulse spectra are displayed. The interaction of these two pulses with the sample results in a probe pulse with sharp gain features (black). A normalized Raman spectrum is produced by taking the natural log of the probe + Raman spectrum divided by the probe only envelope (inset, top).

The FSRS experiment is constructed in such a way as to decouple the time and energy resolution, elegantly circumventing the energy-time uncertainty principle. This concept is illustrated in **Figure 2.3** where the FSRS pulses are displayed in the time domain above an energy level diagram of the FSRS process. The ultrashort actinic pulse excites the molecule, triggering the photochemical process with high temporal precision. The stimulated Raman process is initiated when the Raman and probe pulses coincide within the sample, creating a vibrational coherence on the excited state. Because initiation of the Raman process requires the presence of both the Raman and probe pulses, it is also gated with high temporal precision, limited by the duration of the probe pulse. Further interaction of the sample with the Raman pulse at any time during the vibrational dephasing process results in the coherent emission of Raman shifted photons coincident with the probe. Thus, the time precision of FSRS is determined by the durations of the ultrashort actinic and probe pulses used to *initiate* the photochemistry, and Raman process, respectively. The detection step is fundamentally not time-resolved, as the second interaction with the Raman pulse may occur at any time during its duration, as long as the vibrational coherence has not completely decayed, allowing for excellent vibrational energy resolution.[2–5]

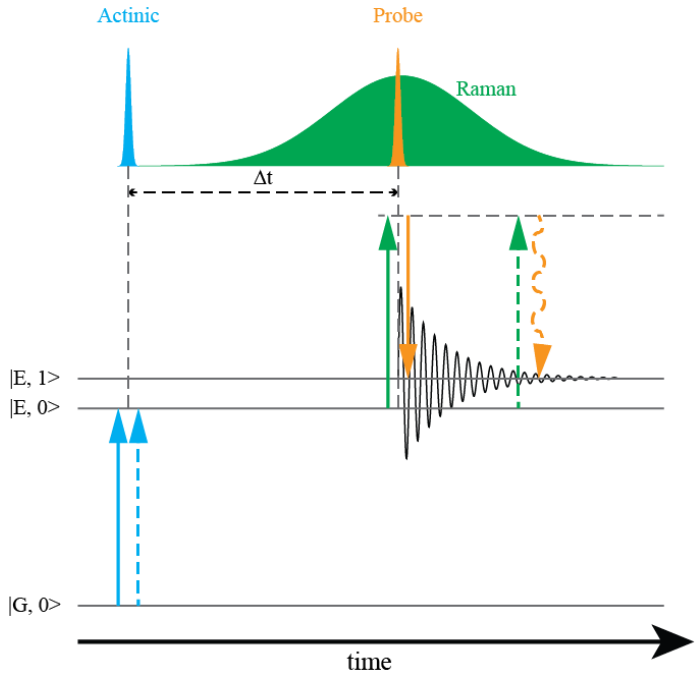

Figure 2.3 The three FSRS pulses are pictured in the time domain above an energy level diagram for the FSRS process. The ultrashort actinic pulse (cyan) promotes the system from the ground state to an excited electronic state. Following a delay of Δt, the Raman (green) and probe (orange) pulses interact with the sample, initiating a vibrational coherence on the excited state. A second interaction with the Raman pulse field during the vibrational dephasing of the coherence results in emission of Raman photons coincident with the probe pulse.

As with spontaneous Raman scattering, FSRS signals are enhanced when the Raman pulse is resonant or preresonant with an electronic transition. Selective enhancement of Raman scattering from specific chromophores is particularly useful when studying photoactive proteins and biological pigments where the primary photochemistry is often localized to a relatively small, light-absorbing moiety, which would otherwise be obscured by the multitude of other protein vibrations. Performing FSRS with a Raman pulse tunable throughout the visible provides the advantage of being able to selectively enhance transient states and chromophores of interest in a variety of photochemical systems. Resonance enhancement also allows FSRS signals to be collected using decreased Raman pulse powers, limiting photo-degradation when studying sensitive biological samples.

Performing FSRS experiments requires a specialized laser system capable of producing the three pulses necessary for the experiment. The following sections describe techniques for generating the FSRS pulses from a single femtosecond Ti:Sapphire regenerative amplifier and the layout and specifications of the tunable FSRS system and detection apparatus. Experimental techniques, sample handling, and prospective improvements are also discussed.

2.2 Generation of Tunable FSRS Pulses

Generating tunable visible pulses is accomplished using a variety of non-linear optical techniques including second harmonic generation (SHG), continuum generation and optical parametric amplification. Designs for the non-linear components used to produce the FSRS pulses are described below.

2.2.1 Probe Pulse

The probe pulse is produced from supercontinuum generation[6] by focusing a small portion of the amplifier output (~ 10 nJ) into a 3 mm thick sapphire window using a 100 mm focal length (FL) spherical lens. The continuum generation optical setup is shown in **Figure 2.4**. Before focusing, the 800 nm beam is directed through an adjustable iris and a gradient neutral density (ND) filter, which are adjusted to optimize the spectral shape and stability of the continuum pulses, and to ensure mono-filamentation of the beam. Following supercontinuum generation in sapphire, the white-light continuum is collimated with a 20 mm FL achromatic doublet producing a ~ 3 mm diameter beam.

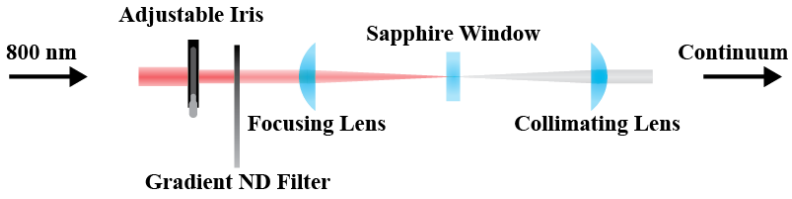

Figure 2.4 The optical setup for supercontinuum generation used to produce the probe pulse. The fundamental is passed through an adjustable iris and gradient ND filter and then focused in a sapphire window. The resulting continuum is optimized by adjusting the diameter and power of the input beam. Following the sapphire window a second lens collimates the continuum beam.

2.2.2 Actinic Pulse

Tunable actinic pulses are generated using a noncollinear optical parametric amplifier (NOPA) based on a design published by Wilhelm et al.[7] A schematic of the NOPA is displayed in **Figure 2.5**. In the NOPA a continuum seed pulse and a 400 nm pump pulse are mixed in a 2-mm thick β-barium-borate (BBO) crystal cut for type I phase matching (26º) to produce amplified, broadband (> 400 cm^{-1}) visible pulses tunable from 460 to 690 nm. Type I phase matching requires horizontally polarized seed and vertically polarized pump pulses, and produces horizontally polarized signal and vertically polarized idler pulses. (It is possible to build a similar NOPA using a type II BBO crystal, yielding idler and signal pulses that are both horizontally polarized.) A small portion of the 800 nm fundamental is focused into a 3 mm thick sapphire window with a 100 mm FL curved mirror. Reflective optics (e.g. curved mirrors for focusing) are used whenever possible in the NOPA to avoid introducing additional group velocity dispersion (GVD) to the pump and seed pulses. As with the probe, the quality of the continuum is optimized by passing the fundamental through an adjustable iris and ND filter prior to focusing. Additionally, an adjustable delay (a retro-reflector on a linear translation stage) is placed on the seed beam-line to allow optimization of the temporal overlap between the pump and seed pulses in the BBO crystal. Following generation, the seed pulse is focused on the BBO

crystal with a 50 mm FL curved mirror. The 400 nm pump pulses for the NOPA are generated through SHG of the fundamental in a 0.2 mm thick BBO crystal (type I, 29.2º). The SHG process conveniently produces vertically polarized 400 nm pulses from the horizontally polarized 800 nm input. The pump pulse is focused on the BBO with a 250 mm FL curved mirror. The focused seed and pump pulses are overlapped spatially and temporally at the front of the BBO crystal where parametric amplification occurs. The NOPA output is tuned and optimized by adjusting the orientation of the BBO crystal (angle tuning of the phase matching condition), and the temporal and spatial overlap of the pump and seed pulses. Following amplification the NOPA output is collimated with a 150 mm FL achromatic doublet. When desired the pump beam for the NOPA may be also used as the source for 400 nm actinic pulses.

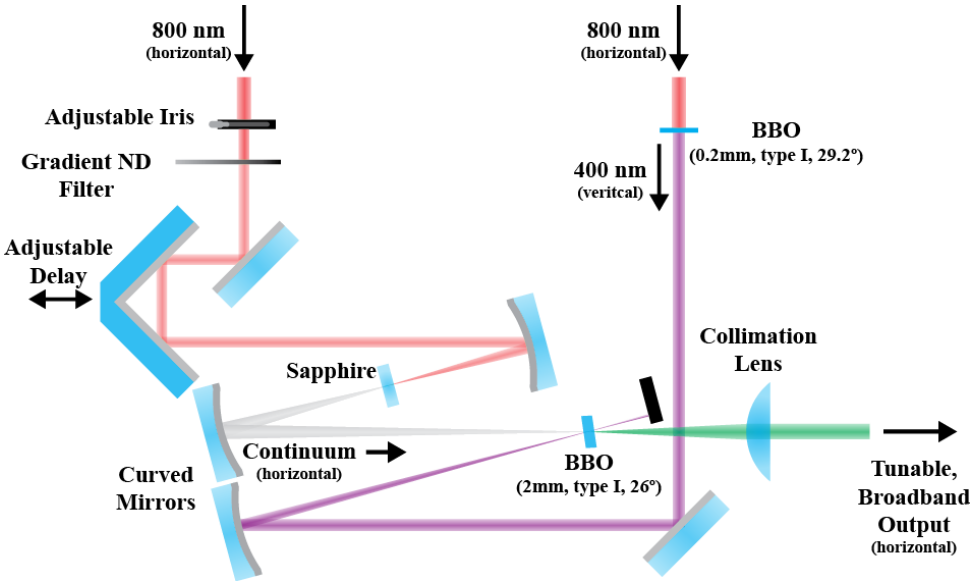

Figure 2.5 Illustration of a non-collinear optical parametric amplifier (NOPA) showing the optics necessary to generate tunable, broadband pulses from the 800 nm output of a Ti:sapphire amplifier.

2.2.3 Raman Pulse

Tunable, narrowband Raman pulses are generated using a special, narrowband optical parametric amplifier (NB-NOPA).[8] The design of the NB-NOPA is analogous to the NOPA design displayed above; a 400 nm pump and visible seed pulse are mixed in a BBO crystal producing an amplified signal. However, the pump and seed pulses for the NB-NOPA are narrowband. The narrowband pump and seed pulses are generated from broadband pulses using double-pass grating filters.[9] An illustration of the grating filter design is shown in **Figure 2.6**. The fundamental (470 µJ) is stretched in a grating filter (200 mm FL, 2200 ln/mm) to produce 45 µJ, ~ 0.6 ps, 800 nm pulses. SFG of these narrowband pulses in an 8 mm BBO (type I, 29.2º) produces ~ 4 µJ narrowband 400 nm pump pulses. Weak, narrowband seed pulses are produced by spectrally filtering the output of a seed NOPA with a second grating filter (100 mm FL, 1800 gr/mm). The narrowband seed and pump pulses are then focused and overlapped spatially and temporally on a 5 mm type I BBO. As with the NOPA, the output of the NB-NOPA is optimized by adjusting the phase matching angle of the BBO, and the temporal and spatial overlap of the

pump and seed pulses. Because the stretched seed pulse is generally longer than the pump pulse, the bandwidth of the NB-NOPA output is generally dominated by the latter, causing slight broadening of the seed pulse upon amplification.[8] Narrowing the bandwidth may be accomplished by decreasing the slit width of the grating filter in the pump beam, however, this also lowers the power of the pump beam, and in turn, the NB-OPA output. Transmissive optics are used in the NB-NOPA (e.g. lenses for focusing, right-angle prisms for retro-reflecting) as GVD is negligible for narrowband pulses, and they are generally easier to maintain. The NB-NOPA output is collimated with a 130 mm spherical lens. The narrowband 400 nm pulses that pump the NB-NOPA may also be used themselves as the Raman pulse. Raman pulses produced in this way will be vertically polarized and will need to have their polarization rotated to horizontal using a λ/2 wave plate to match that of the probe to acquire polarized Raman spectra.

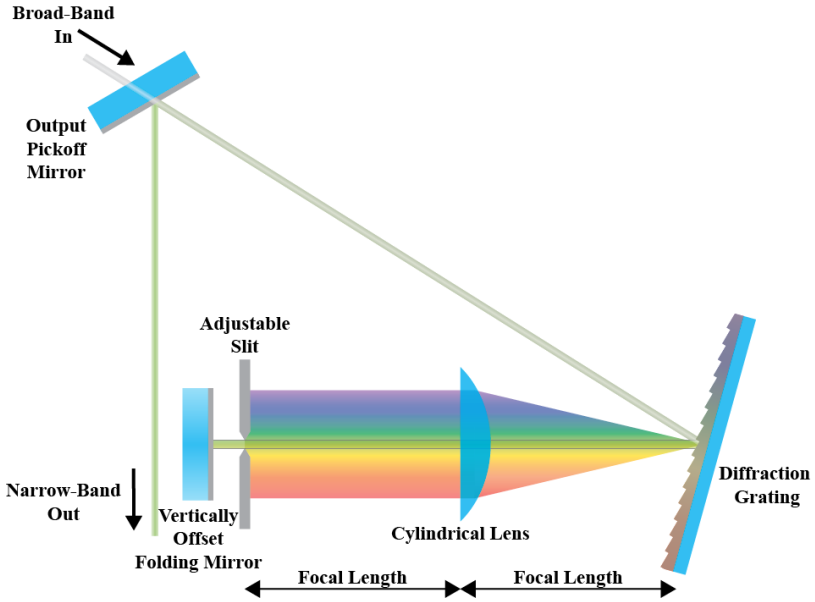

Figure 2.6 Illustration of a double-pass grating filter used to generate narrowband pulses from broadband pulses. A broadband beam is dispersed off of a reflective grating. The 1st order diffraction is focused onto an adjustable slit by a cylindrical lens centered between the grating and slit, one focal length away from each. A mirror placed after the slit retro-reflects the spectrally filtered beam with a slight vertical offset to allow isolation with a pick-off mirror.

2.3 Tunable FSRS Laser System

A schematic of the layout of the tunable FSRS system is shown in **Figure 2.7**. Though the figure is highly simplified and not to scale, it serves as a fairly accurate road map to the instrument. The system has been adapted from the design originally published by Shim et al.[10] The detection system has been vastly improved by adding a fast CCD that can record each pulse's spectrum at a kHz rep-rate allowing for the study of weakly scattering chromophores. Additionally the layout of the optical bench has been redesigned to improve stability, compression of the actinic and probe pulses, and to simplify the setup of the experiment. The current configuration of this system is described in detail below.

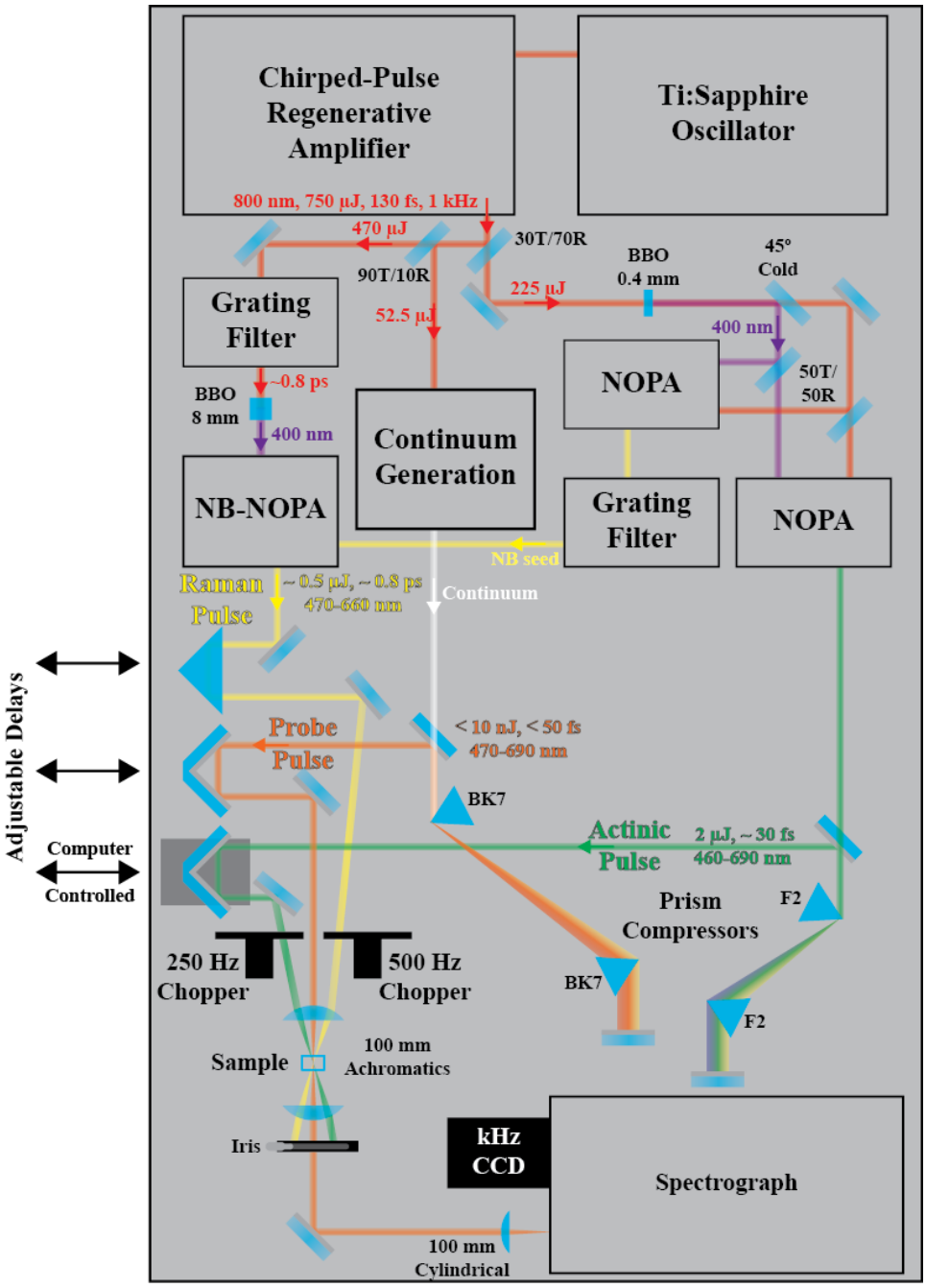

Figure 2.7 Illustration of the tunable FSRS system showing the relative arrangement of the components in the optical setup, and specifications of the various beam lines. Beam-splitters are labeled showing their transmission and reflection efficiencies (e.g. 30T/70R represents a beam-splitter which is 30% transmissive and 70% reflective).

The laser system for tunable FSRS is driven by a Ti:sapphire chirped-pulse regenerative amplifier (Spectra Physics, Spitfire) seeded by a home-built Kerr lens mode-locked oscillator.[11,12] The 1 kHz amplifier produces a train of 750 μJ, 130 fs 800 nm pulses. This output is split into several beams in order to generate the tunable FSRS pulses. The two NOPAs used to generate the actinic pulse, and to seed the NB-OPA are driven with 225 μJ of the amplifier output isolated using a broadband beam-splitter (30% transmissive, 70% reflective). Each NOPA requires a beam of vertically polarized, 400 nm pump pulses and a beam of horizontally polarized 800 nm pulses. Vertically polarized 400 nm pump pulses are produced by SHG of the horizontally polarized amplifier fundamental in a 0.4 mm BBO crystal (type I, 29.2º). To make efficient use of the amplifier output, the 400 nm pulses are isolated from the residual, 800 nm fundamental with a 45º cold mirror (reflects wavelengths < 700 nm, transmits wavelengths > 700). The resulting 40 μJ 400 nm and 120 μJ 800 nm beams are each split using 50% transmissive, 50% reflective beam-splitters to provide the input beams for each of the two NOPAs. The output of one NOPA is passed through a grating filter to produce the narrowband seed used to produced the Raman pulse, while the output of the other is compressed in a pair of equilateral dispersing prisms (F2) to produce the ultrafast actinic pulse. Compression of the actinic pulse is characterized by directing the beam into a home-built SHG autocorrelator.[13,14]

The remainder of the amplifier output is used to generate the Raman and probe pulses. A 90% transmissive, 10% reflective beam-splitter isolates a ≈ 50 μJ of the fundamental for continuum generation. Following generation in sapphire, the continuum probe pulse is compressed in a pair of equilateral dispersing prisms (BK7). This prism compressor conveniently serves as a spatial band-pass filter, and is also used to tune the probe to the red edge of the Raman pulse. The chirp of the probe pulse and instrument response are characterized and optimized by optical Kerr effect cross correlation with the actinic pulse in the sample cell.[15,16]

The remaining 470 μJ of fundamental is stretched in a grating filter, followed by doubling to produce the narrowband 400 nm pump beam for the NB-OPA. This pump beam is mixed with the grating filtered output of the seed NOPA to produce the Raman pulse.

The actinic, Raman, and probe pulses each pass through an adjustable delay line before being conveyed to the sample point. A single achromatic doublet focuses the three pulses on the sample, where they are spatially, and temporally overlapped. After the sample, the probe beam is collimated and passes through an iris that blocks the actinic and Raman pulses. A cylindrical 100 mm cylindrical lens focuses the probe on the entrance slit of the spectrograph (500 M, Spex, 600 gr/mm) where it is dispersed onto a 1 kHz, front-illuminated CCD (Pixis 100F, Princeton Instruments).

2.4 Detection

The FSRS spectra are collected by modulating the three pulses in precise order to produce normalized Raman gain spectra for the sample in the ground state, and after actinic excitation. The 1 kHz CCD records every probe pulse, while two phase locked choppers (also synched to the amplifier output) modulate the actinic and Raman pulses at 250 and 500 Hz, respectively. This pulse sequence is shown in **Figure 2.8** on the left, and the mathematical relations between the various signals produced by the four pulse combinations and the spectra they are used to produce is shown on the right. By modulating the actinic and Raman pulses in

this way it is possible to acquire ground state FSRS along with excited FSRS and transient absorption for a given time delay in 4 laser shots, or 4 ms. The collection of these spectra is automated by a LabVIEW program, and a D-type flip-flop circuit connected between the choppers and the CCD trigger is used to ensure the detection sequence begins at the same point in the pulse sequence each time. The LabVIEW program also controls the linear stage (M405.DG, Physik Instrumente) used to automate the delay between the actinic and probe pulses.

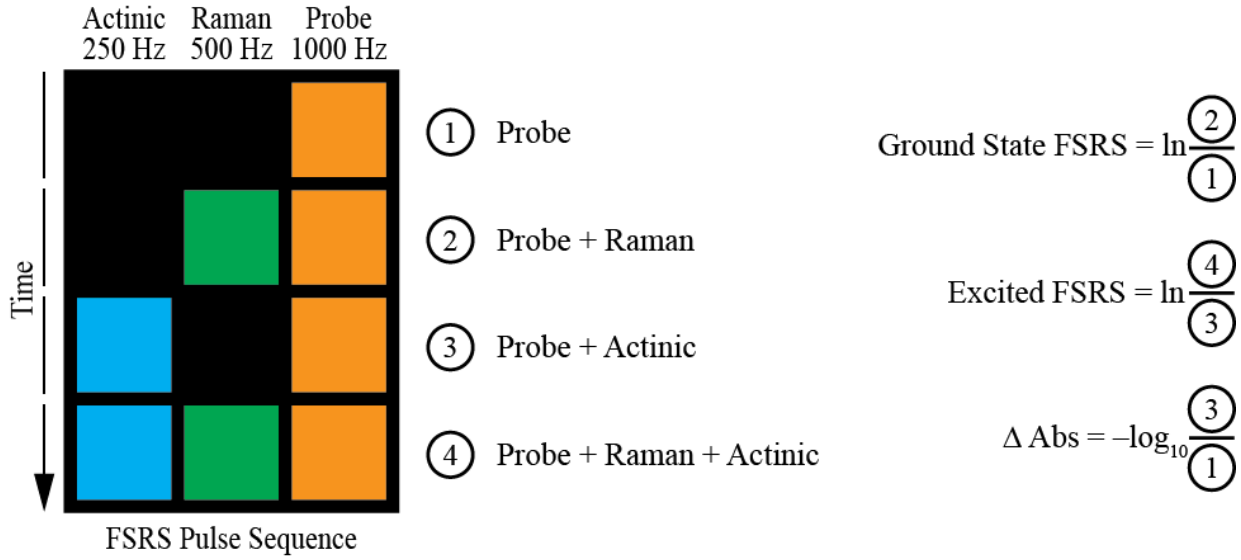

Figure 2.8 The pulse timing sequence for FSRS detection. A block diagram representing the pulses is displayed on the left. Colored squares indicates the presence of a pulse on the sample. The actinic pulse is displayed in cyan, the Raman pulse in green, and the probe pulse in orange. On the right the relation of the signals collected to their corresponding spectra is shown.

2.5 Sample Handing

Performing time resolved experiments requires replenishment of the sample between laser shots in order to avoid buildup of photo-converted sample in the beam path. The duration of the photoaltered state, and the photoalteration rate of the sample determine the rate of replenishment, and if recirculation, or single pass flowing of the sample is necessary. Replenishment is typically accomplished by flowing the sample. It is preferable to use a sample cell with a short path length (1 mm or less) and thin windows in order to minimize GVD introduced by the sample. Peristaltic pumps are the preferred method of flowing. Because the sample only comes in contact with replaceable tubing, peristaltic pumps are easy to maintain, adaptable to a variety of chemicals, and can be used to convey small volumes.

The ability to handle small volumes of sample is crucial when studying synthetic or biological materials of limited availability. When the volume of sample available is too low for even peristaltic flowing, a convenient method of ensuring sample replenishment is the use of a small magnetic stir bar in a small volume cuvette. When stirring is not feasible automated translation of a sample fixed in a planar cell can be used for replenishment.

2.6 Experimental Considerations

When choosing the wavelengths for the FSRS pulses there are various parameters to consider in order to ensure a successful measurement. Tuning the actinic pump is rather simple: it is tuned to the ground state resonance of interest. However, placement of the Raman and probe pulses is somewhat more difficult. In addition to the desired FSRS process, several other nonlinear pathways may also contribute to the observed signals, especially when the Raman and probe pulses are strongly resonant with different electronic states.[3,5,17–19]

Because of the way the FSRS spectra are detected (**Figure 2.8**), when the Raman and probe pulses are resonant with an electronic transition, population changes (excitation or dumping) induced by the Raman pulse produce strong, complicated, baselines.[20] Furthermore, under these conditions additional photophysical pathways contribute to the observed signals, resulting in complex spectral lineshapes.[17,19] To minimize and avoid these effects it is advantageous to tune the Raman and probe pulses preresonant of the fluorescence band. In addition to avoiding strong resonance with the stimulated emission band, it is also desirable to probe preresonant of any known excited state absorptions due to competing non-linear pathways. These principles are illustrated in **Figure 2.9**. Although it may be necessary to stray from these recommended conditions for some studies, they are generally a good starting point when designing FSRS experiments for new systems.

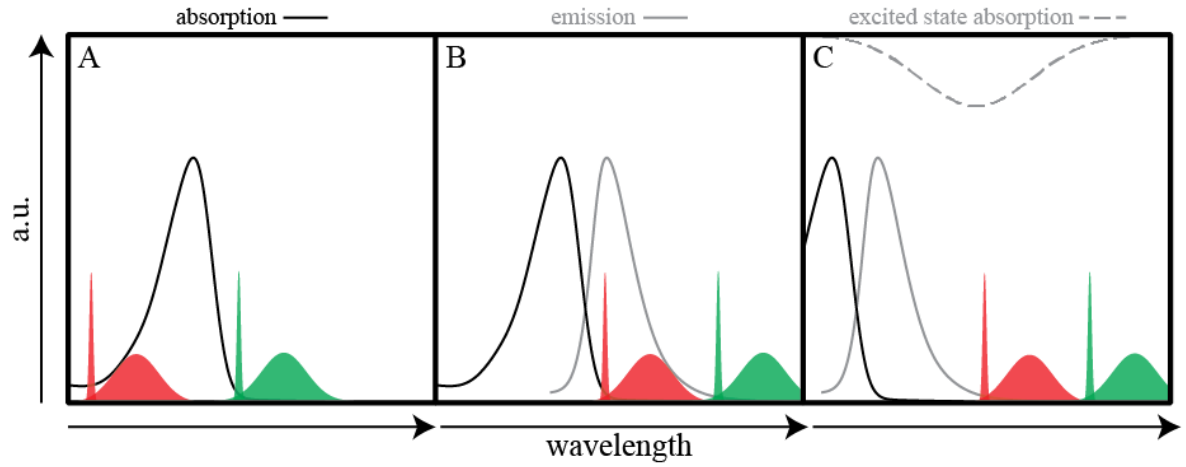

Figure 2.9 Recommended tuning of the Raman and probe pulses for stokes FSRS experiments. The Raman pulse is represented by a narrow, filled Gaussian. The probe pulse is represented by a broad, filled Gaussian on the low-energy edge of the Raman pulse. Recommended conditions are shown in green, while potentially unfavorable conditions are shown in red. **A**: Probing on the low-energy edge of the absorption band (green) will avoid excitation of the sample by the Raman and probe pulses, as well as extinction of the probe pulse by the sample (red). **B**: When performing time-resolved experiments on fluorescent samples probing on the low-energy edge of the emission band (green) will reduce interference resulting from dumping pathways (red). **C**: Probing on the low-energy edge of transient absorption bands of interest (green) is recommended to avoid complex signals produced when probing within an electronic transition (red).

2.7 Prospective Improvements

The perturbative effect of the Raman pulse on the excited state population is exacerbated by its Gaussian temporal profile. Photons from the Raman pulse interact with the actinically pumped sample for approximately half of its duration before the probe initiates the Raman process. In addition to perturbing the system under study, the Raman pulse photons that impinge on the sample prior to the arrival of the probe pulse add nothing to the FSRS signal. It has recently been shown that Raman pulses with an optimal temporal profile may be produced using a Fabrey-Pérot etalon filter.[20] It should be possible to produce a similar effect by using an etalon filter to generate the pump pulse for the NB-NOPA. The resulting amplified pulse will adopt the the rapid rise and exponential decay characteristic of the etalon filtered pump pulse. Using Raman pulses with this asymmetric temporal profile has been shown to reduce the pre-probe interactions with the excited state population resulting in improved baselines.[20]

An improved design for the grating filter used to generate the narrowband seed pulse could also potentially improve the performance of the NB-NOPA. Replacing the current 500 nm blazed grating with a holographic grating designed for high efficiency over a broad wavelength range would improve the performance at wavelengths farther from 500 nm, potentially increasing the effective tuning range. Furthermore, it is possible to obtain holographic gratings with very high line densities. Using such a grating would increase the angular dispersion of the broadband pulse in the filter, allowing for a wider slit width resulting in less beam distortion, and higher wavelength selectivity.

2.8 References

(1) McCamant, D. W.; Kukura, P.; Yoon, S.; Mathies, R. A. Femtosecond Broadband Stimulated Raman Spectroscopy: Apparatus and Methods. *Rev. Sci. Instrum.* **2004**, *75*, 4971–4980.

(2) Kukura, P.; Yoon, S.; Mathies, R. A. Femtosecond Stimulated Raman Spectroscopy. *Anal. Chem.* **2006**, *78*, 5952–5959.

(3) Frontiera, R. R.; Mathies, R. A. Femtosecond Stimulated Raman Spectroscopy. *Laser Photonics Rev.* **2011**, *5*, 102–113.

(4) Lee, S.-Y.; Zhang, D.; McCamant, D. W.; Kukura, P.; Mathies, R. A. Theory of Femtosecond Stimulated Raman Spectroscopy. *J. Chem. Phys.* **2004**, *121*, 3632.

(5) Sun, Z.; Lu, J.; Zhang, D. H.; Lee, S.-Y. Quantum Theory of (femtosecond) Time-Resolved Stimulated Raman Scattering. *J. Chem. Phys.* **2008**, *128*, 144114–144113.

(6) Brodeur, A.; Chin, S. L. Ultrafast White-Light Continuum Generation and Self-Focusing in Transparent Condensed Media. *J. Opt. Soc. Am. B* **1999**, *16*, 637–650.

(7) Wilhelm, T.; Piel, J.; Riedle, E. Sub-20-Fs Pulses Tunable Across the Visible from a Blue-Pumped Single-Pass Noncollinear Parametric Converter. *Opt. Lett.* **1997**, *22*, 1494–1496.

(8) Shim, S.; Mathies, R. A. Generation of Narrow-Bandwidth Picosecond Visible Pulses from Broadband Femtosecond Pulses for Femtosecond Stimulated Raman. *Appl. Phys. Lett.* **2006**, *89*, 121124.

(9) Martinez, O. E. 3000 Times Grating Compressor with Positive Group Velocity Dispersion: Application to Fiber Compensation in 1.3-1.6 μm Region. *IEEE J. Quantum Electron.* **1987**, *23*, 59–64.

(10) Shim, S.; Mathies, R. A. Development of a Tunable Femtosecond Stimulated Raman Apparatus and Its Application to B-Carotene. *J. Phys. Chem. B* **2008**, *112*, 4826–4832.

(11) Asaki, M. T.; Huang, C.-P.; Garvey, D.; Zhou, J.; Kapteyn, H. C.; Murnane, M. M. Generation of 11-Fs Pulses from a Self-Mode-Locked Ti:sapphire Laser. *Opt. Lett.* **1993**, *18*, 977–979.

(12) Murnane, M. M.; Kapteyn, H. C.; Huang, C.-P.; Asaki, M. T. Modelocked Ti:sapphire Laser, **1994**.

(13) Herrmann, J. Methods of Measurement. In *Lasers for ultrashort light pulses*; North-Holland ; Distributors for the U.S.A. and Canada, Elsevier Science Pub. Co: Amsterdam ; New York : New York, NY, **1987**; pp. 91–117.

(14) Demtröder, W. Time-Resolved Laser Spectroscopy. In *Laser Spectroscopy*; Springer Berlin Heidelberg, **2008**; Vol. 2, pp. 259–350.

(15) Fleming, G. R. *Chemical Applications of Ultrafast Spectroscopy*; Oxford University Press, Incorporated, **1986**.

(16) Yamaguchi, S.; Hamaguchi, H.-O. Convenient Method of Measuring the Chirp Structure of Femtosecond White-Light Continuum Pulses. *Appl. Spectrosc.* **1995**, *49*, 1513–1515.

(17) McCamant, D. W.; Kukura, P.; Mathies, R. A. Femtosecond Stimulated Raman Study of Excited-State Evolution in Bacteriorhodopsin. *J. Phys. Chem. B* **2005**, *109*, 10449–10457.

(18) Frontiera, R. R.; Shim, S.; Mathies, R. A. Origin of Negative and Dispersive Features in Anti-Stokes and Resonance Femtosecond Stimulated Raman Spectroscopy. *J. Chem. Phys.* **2008**, *129*, 064507–6.

(19) Nakamura, R.; Hamada, N.; Abe, K.; Yoshizawa, M. Ultrafast Hydrogen-Bonding Dynamics in the Electronic Excited State of Photoactive Yellow Protein Revealed by Femtosecond Stimulated Raman Spectroscopy. *J. Phys. Chem. B* **2012**, *116*, 14768–14775.
(20) Hoffman, D. P.; Valley, D.; Ellis, S. R.; Creelman, M.; Mathies, R. A. Optimally Shaped Narrowband Picosecond Pulses for Femtosecond Stimulated Raman Spectroscopy. *Opt. Express* **2013**, *21*, 21685–21692.

Chapter 3

Femtosecond Time-Resolved Optical and Raman Spectroscopy of Photoinduced Spin Crossover: Temporal Resolution of Low-to-High Spin Optical Switching

3.1 Abstract

A combination of femtosecond electronic absorption and stimulated Raman spectroscopies has been employed to determine the kinetics associated with low-spin to high-spin conversion following charge-transfer excitation of an iron(II) spin-crossover system in solution. A time constant of $\tau = 190 \pm 50$ fs for the formation of the $^5T_2$ ligand-field state was assigned based on the establishment of two isosbestic points in the ultraviolet in conjunction with changes in ligand stretching frequencies and Raman scattering amplitudes; additional dynamics observed in both the electronic and vibrational spectra further indicate that vibrational relaxation in the high-spin state occurs with a time constant of ca. 10 ps. The results set an important precedent for extremely rapid, formally forbidden ($\Delta S = 2$) nonradiative relaxation as well as defining the time scale for intramolecular optical switching between two electronic states possessing vastly different spectroscopic, geometric, and magnetic properties.

3.2 Introduction

Understanding the mechanisms by which molecules interconvert among their distinct electronic and/or geometric configurations in response to external perturbations constitutes an important step toward the development of molecular-based materials.[1,2] Low-spin iron(II) complexes comprise an intriguing class of compounds in this regard due to their potential utility in solar energy conversion strategies[3,4] as well as the basis for magneto-optical devices.[5] It is well-known that photoexcitation of such compounds results in the eventual formation of the high-spin form of the molecule; the net two-quantum spin conversion coincides with an exceptionally large structural reorganization ($\Delta r_{Fe-L} \sim 0.2$ Å, $\Delta V \sim 25$ cm^3 mol^{-1}), significant attenuation of the compound's optical density ($\Delta\epsilon \sim 10^3$ M^{-1} cm^{-1}), and a dramatic change in the compound's magnetic properties ($S = 0 \rightarrow S = 2$).[6] Several groups have exploited various spectroscopic probes in an effort to quantify the dynamics of this spin-state conversion but thus far have only been able to define an upper limit for the time constant associated with formation of the high-spin state.[7–10] In this report, we present femtosecond optical and stimulated Raman

scattering data on a prototypical low-spin iron(II) charge-transfer complex that, for the first time, kinetically resolves the formation of the high-spin state and thus defines the time scale for optical switching in this class of compounds.

The compound under study is $[Fe(tren(6\text{-}R\text{-}py)_3)]^{2+}$ (R = H (**1**), CH_3 (**2**)), which is illustrated in **Figure 3.1** along with a simplified energy level diagram showing the low-lying ligand-field excited states of a d^6 transition metal ion. As shown by Drago and co-workers,[11] this compound sits very close to the so-called spin-crossover point wherein the energies of the low-spin ($^1A_1$) and high-spin ($^5T_2$) forms are in close proximity. Compound **1** possesses a low-spin ground state, whereas the steric constraints imposed by the introduction of the CH_3 groups in compound **2** require an elongation of the Fe−N bond, resulting in stabilization of the high-spin $^5T_2$ term as its ground state. This system thus has the unique characteristic of having reciprocal ground and lowest-energy excited states; i.e., the lowest-energy excited state of one corresponds to the ground state of the other. We have previously exploited this feature to probe the ultrafast electronic absorption spectroscopy of $[Fe(tren(py)_3)]^{2+}$ in the visible region and have shown that charge-transfer excitation of this compound results in the formation of the $^5T_2$ state in < 1 ps.[7]

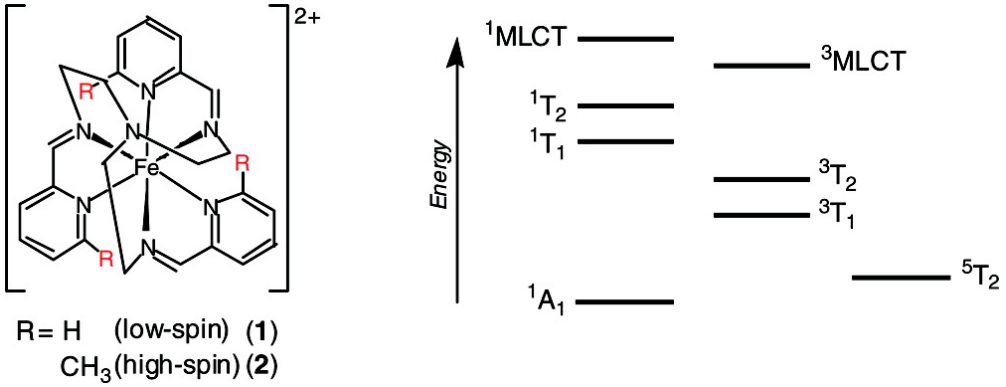

Figure 3.1 Drawing of $[Fe(tren(6\text{-}R\text{-}py)_3)]^{2+}$ (Left), along with a qualitative Jablonski diagram for compound **1** showing the charge-transfer and low-lying ligand-field states (Right).

3.3 Results and Discussion

Owing to the nature of the absorption spectra of the low-spin and high-spin forms of the molecule, more diagnostic features can be found in the ultraviolet region of the spectrum. Specifically, there exist two isosbestic points between the $^1A_1$ and $^5T_2$ states at 285 ± 5 nm and 320 ± 5 nm as indicated by the calculated differential absorption spectrum between compounds **1** and **2** as well as data from nanosecond time-resolved absorption spectroscopy (**Figure 3.2**). (See Appendix A for experimental details.) These observations constitute important optical markers for establishing the formation of the $^5T_2$ excited state of compound **1** following photoexcitation, since it is highly unlikely that three (or more) electronic states of a given molecule will simultaneously possess two coincident isobestic points.

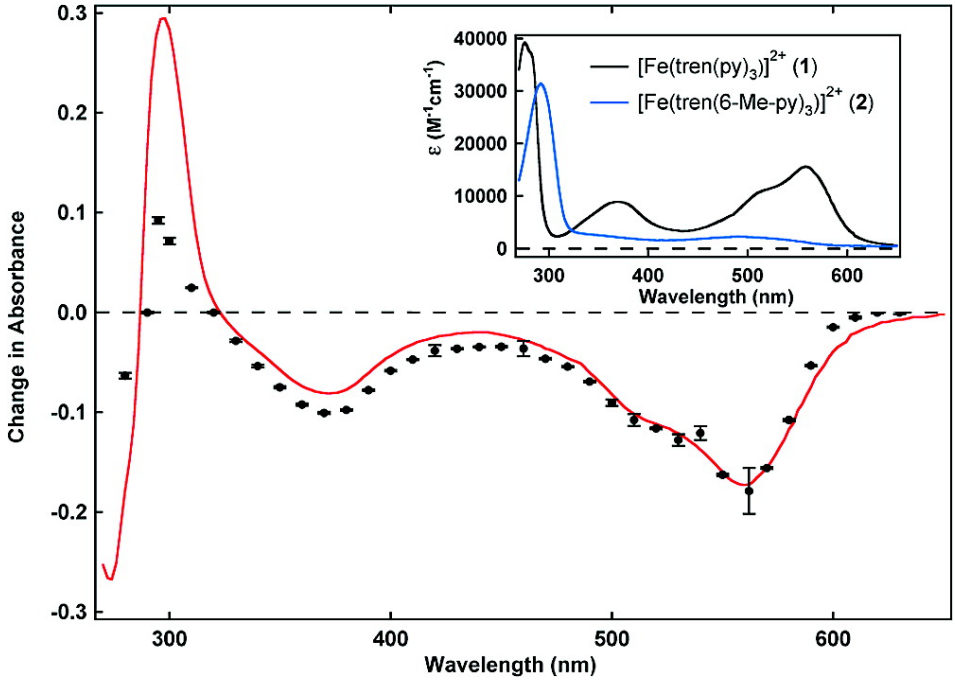

Figure 3.2 Differential absorption spectra for $[Fe(tren(6\text{-}R\text{-}py)_3)](PF_6)_2$ in CH_3CN solution. The data points correspond to amplitudes from fits of nanosecond time-resolved absorption data acquired following $^1A_1 \rightarrow {}^1$MLCT excitation of compound **1** (R = H) at 560 nm, whereas the solid red line is a difference spectrum calculated from the ground-state absorption spectra of compounds **1** and **2** (inset). Wavelengths for which the change in absorbance is zero correspond to isosbestic points between the $^1A_1$ and $^5T_2$ electronic states of this system.

Accordingly, we have acquired femtosecond time-resolved differential absorption data in the ultraviolet region in order to determine at what point in time the low-spin/high-spin isosbestics of compound **1** are established. Measurements were carried out at probe wavelengths on both sides of the two isosbestic points and are shown in **Figure 3.3**. (Experimental details presented in Appendix A.) The data at earliest times are complicated by the presence of features associated with the initially formed metal-to-ligand charge-transfer excited state. Previous work has demonstrated that the lifetime of the charge-transfer manifold of this system is ca. 100 fs.[7] The rise and rapid decay in absorbance that is evident at 315 and 325 nm as well as the partial recovery of the signal at 285 nm can thus be attributed to this charge-transfer excited state based on their temporal profile[7] in conjunction with spectroelectrochemical data obtained for compound **1** (**Figure A.1**).

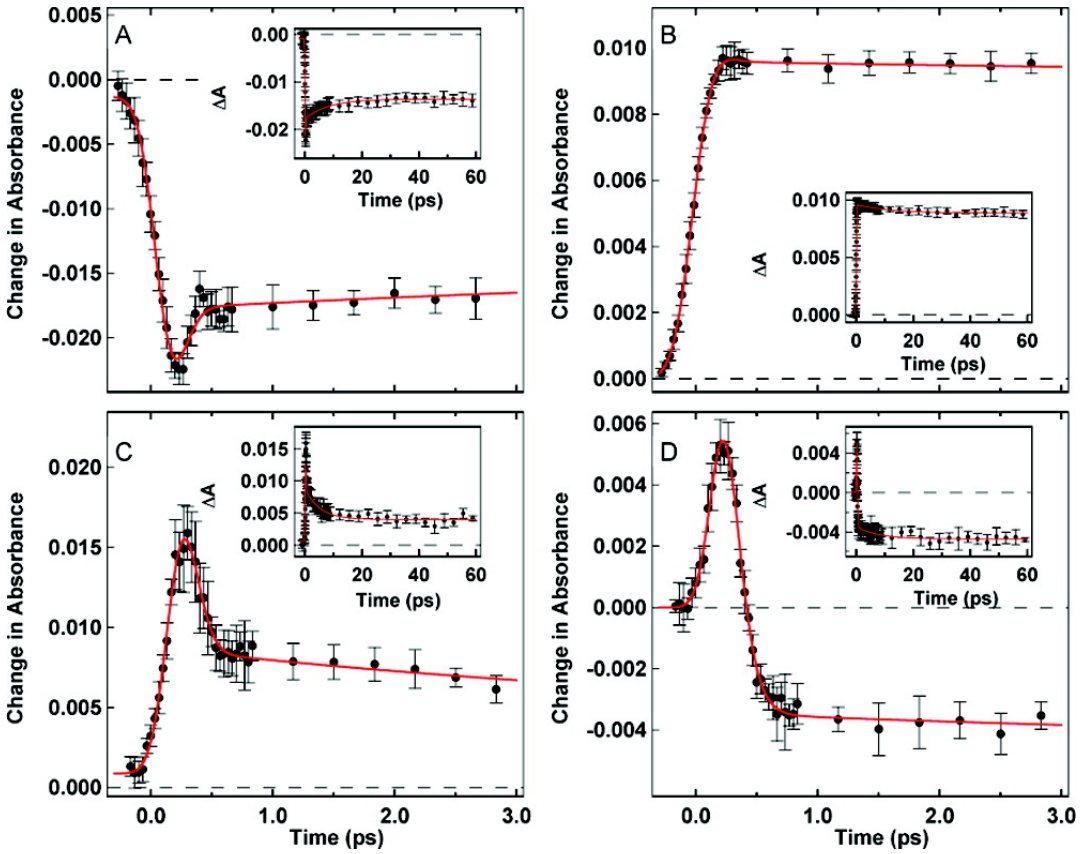

Figure 3.3 Femtosecond time-resolved differential absorption data for $[Fe(tren(py)_3)](PF_6)_2$ (compound **1**) in CH_3CN solution. Data were acquired at 285 (A), 290 (B), 315 (C), and 325 nm (D) following $^1A_1 \rightarrow {}^1$MLCT excitation at 560 nm. The solid lines correspond to fits derived from a convolution of the instrument response function with a biexponential kinetic model ($\tau_1 <$ 250 fs and $\tau_2 = 5.5 \pm 1.5$ ps). See text for further details.

Notwithstanding these charge-transfer features, the data clearly show changes in the sign of the transient absorption signals at either side of the isosbestic points noted in **Figure 3.2**. Specifically, the net loss of absorbance at 285 nm coupled with the positive signal observed at 290 nm indicates that a zero-crossing (i.e., a point at which $\Delta A = 0$) must occur between these two wavelengths. Similarly, a ground-state/exited-state isosbestic also exists between 315 and 325 nm. These spectral ranges coincide precisely with the low-spin/high-spin isosbestic points anticipated for $[Fe(tren(py)_3)]^{2+}$. Our cross-correlation pulse width of 250 fs prohibits an accurate assessment of the kinetics, but the simultaneous presence of both sign changes anticipated from the calculated and nanosecond differential absorption spectra for $[Fe(tren(py)_3)]^{2+}$ provides compelling evidence that the $^5T_2$ state for this molecule is formed in $\tau < 250$ fs.

The actual time constant for high-spin formation was obtained from femtosecond stimulated Raman scattering (FSRS) experiments.[12] Analysis of the data was facilitated by comparing the time-resolved spectra with steady-state resonance Raman data acquired for both the low-spin parent compound **1** and its high-spin analogue, compound **2**; the latter provided an important benchmark for correlating the time-resolved data with the identity of the electronic

state from which it originated. The steady-state and time-resolved spectra are plotted in **Figure 3.4**; kinetic traces corresponding to both spectral position and amplitude are shown in **Figure 3.5**. The most diagnostic region of the spectrum lies above 1600 cm^{-1}: the highest energy band, assigned to the Schiff base C=N stretch of the ligand, undergoes a hypsochromic shift of ca. 33 cm^{-1} between the low-spin and high-spin forms. This is consistent with the attenuation of π-backbonding expected following conversion from the (nominally) t_{2g}^6 electronic configuration associated with the $^1A_1$ state to the $t_{2g}^4e_g^2$ configuration of the high-spin species.

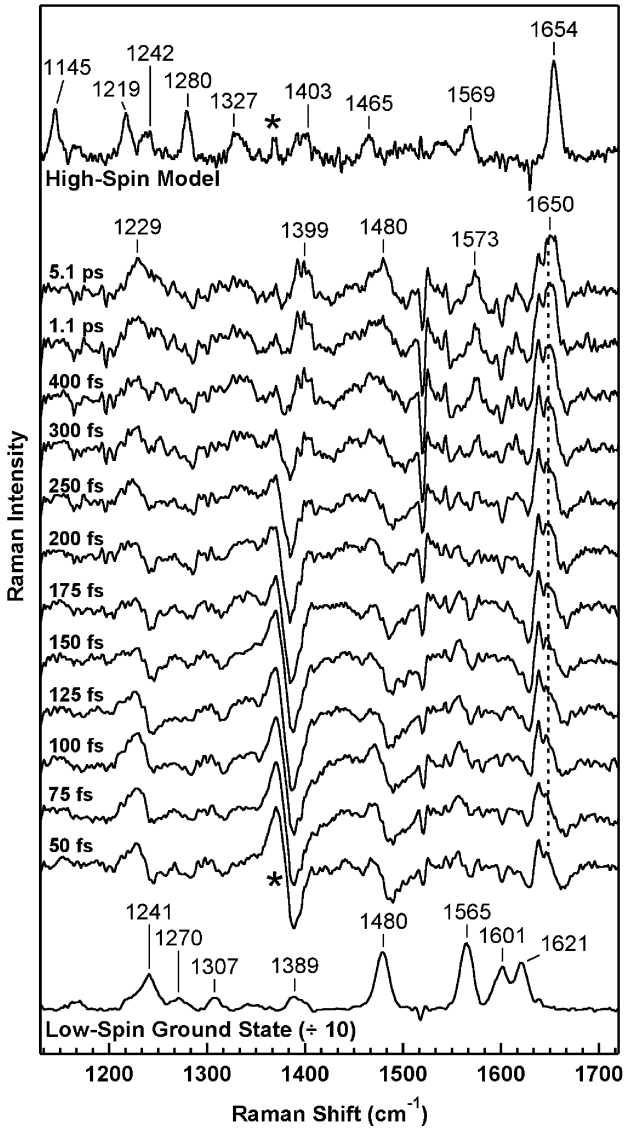

Figure 3.4 Femtosecond stimulated Raman scattering spectra for $[Fe(tren(py)_3)](PF_6)_2$ (compound **1**) in CH_3CN solution. Electronic excitation was carried out at 560 nm with a Raman pump pulse centered at 792 nm. Steady-state Raman spectra for compounds **1** and **2** are shown at the bottom and top of the figure, respectively; inset numbers to the left of the stacked spectra correspond to delay times of the Raman pump relative to the excitation pulse. The dispersive feature at 1376 cm^{-1} (indicated by *) is due to the solvent. Additional experimental details can be found in Appendix A.

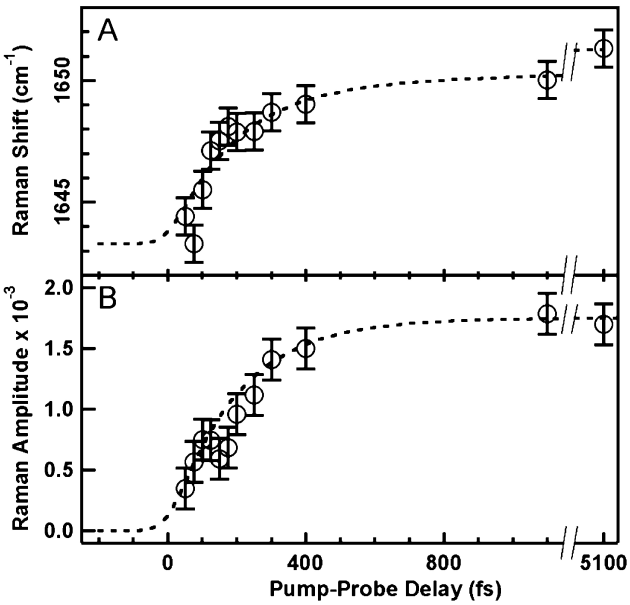

Figure 3.5 Time dependence of the change in energy (A) and spectral amplitude (B) of the C=N stretching vibration of $[Fe(tren(py)_3)](PF_6)_2$ (compound **1**) derived from the femtosecond stimulated Raman scattering data shown in **Figure 3.4**. The dashed lines correspond to fits to exponential kinetic models. Both the spectral shift and amplitude can be modeled with the same initial time constant $\tau = 190 \pm 50$ fs; the spectral shift exhibits a second component with $\tau_2 = 10 \pm 3$ ps. See text for further details.

Excitation into the ^{1}MLCT excited state results in a formal oxidation of the metal center to iron(III) and reduction of the pyridyl ring(s): the appearance of the C=N stretch to the blue side of the ground-state value of 1621 cm^{-1} at $\Delta t = 50$ fs therefore likely reflects this photoinduced shift in charge density, as does the slight red shift of the pyridyl ring C=C and/or C=N stretch(es) at 1460 cm^{-1}. The presence of the CH_3 group in compound **2** is expected to shift the pyridyl ring vibrations in the ca. 1450−1550 cm^{-1} region to somewhat lower energies relative to compound **1**. As the spectrum evolves, a feature near 1650 cm^{-1} characterized by a progression to higher energy develops during the first ca. 500 fs followed by a more gradual change on a longer (i.e., picosecond) time scale. The shift in the maximum of this band can be accurately described using a biphasic exponential model with time constants $\tau_1 = 190 \pm 50$ fs and $\tau_2 = 10 \pm 3$ ps (**Figure 3.5A**). Given that the electronic evolution of the compound is complete in < 250 fs (**Figure 3.3**), τ_2 can be confidently assigned to vibrational relaxation within the $^5T_2$ ligand-field state. The value is within experimental error of the second kinetic component used to model the data in **Figure 3.3** as well as our previous observations from electronic absorption spectroscopy on compound **1**.[7] Similar conclusions have been drawn from femtosecond time-resolved infrared data on other systems, reflecting an emerging consensus on the approximate time scale for vibrational relaxation in coordination compounds.[13–15]

The fact that the formation of both isosbestic points occurs on a time scale similar to τ_1 suggests that these kinetics are diagnostic of the structural evolution associated with the low-to-high spin conversion; the time-dependent shift of the C=N stretching frequency to higher energy reflects the aforementioned reduction in metal−ligand back-bonding that is expected to occur

concomitant with the formation of the $^5T_2$ state. A relaxation pathway of ^{1}MLCT → ^{3}MLCT → $^5T_2$ has been identified for $[Fe(bpy)_3]^{2+}$.[10] In the present case, only a single process (i.e., τ_1) reflecting the overall conversion to the $^5T_2$ state was resolved. This assignment is further supported by the temporal profile of the Raman amplitude (**Figure 3.5B**). Specifically, the increase in amplitude, which exhibits kinetics identical to the spectral shift described by τ_1, indicates an increase in the polarizability of the chromophore. This is consistent with a low-to-high spin conversion due to the larger molecular volume and smaller metal−ligand force constants associated with the $^5T_2$ state. The lack of a second component in the time−amplitude trace is likewise consistent with this picture given that vibrational cooling is occurring on the $^5T_2$ surface, i.e., subsequent to the major electronic and structural changes of the system.

3.4 Conclusion

The results presented herein have several important implications. First, from a fundamental perspective, the fact that a net $\Delta S = 2$ conversion has been quantified with a rate constant of ca. 5×10^{12} s^{-1} raises interesting questions in terms of the applicability of existing theoretical formalisms for describing nonradiative decay dynamics in molecular systems.[10] Second, the formation of low-lying ligand-field states has been implicated as an important decay pathway limiting the utility of transition metal-based chromophores in certain solar energy conversion strategies:[7,8] the data we have obtained serve to define an important kinetic benchmark in this regard. Lastly, the applicability of spin-crossover systems to optical device development relies in part on rapid, efficient photoinduced interconversion between the low-spin and high-spin states.[5] Our results suggest that switching times for devices employing such compounds could be extremely rapid. Efforts to probe these questions as well as assess the generality of the results we have presented are ongoing.

3.5 Acknowledgement

This work was supported by the Chemical Sciences, Geosciences, and Biosciences Division, Office of Basic Energy Sciences, U.S. Department of Energy Grant No. DE-FG02-01ER15282 (J.K.M.), and the Mathies Royalty Fund (R.A.M.).

3.6 References

(1) Balzani, V.; Credi, A.; Venturi, M. Molecular Devices and Machines. *Nano Today* **2007**, *2*, 18–25.

(2) Kay, E. R.; Leigh, D. A.; Zerbetto, F. Synthetic Molecular Motors and Mechanical Machines. *Angew. Chem. Int. Ed.* **2007**, *46*, 72–191.

(3) Ferrere, S.; Gregg, B. A. Photosensitization of TiO_2 by $[Fe^{II}(2,2'\text{-Bipyridine-}4,4'\text{-Dicarboxylic acid})_2(CN)_2]$: Band Selective Electron Injection from Ultra-Short-Lived Excited States. *J. Am. Chem. Soc.* **1998**, *120*, 843–844.

(4) Meyer, G. J. Molecular Approaches to Solar Energy Conversion with Coordination Compounds Anchored to Semiconductor Surfaces. *Inorg. Chem.* **2005**, *44*, 6852–6864.

(5) Létard, J.-F. Photomagnetism of iron(II) Spin Crossover Complexes—the T(LIESST) Approach. *J. Mater. Chem.* **2006**, *16*, 2550–2559.

(6) *Spin Crossover in Transition Metal Compounds I*; Gütlich, P.; Goodwin, H. A., Eds.; Topics in Current Chemistry; 2004.

(7) Monat, J. E.; McCusker, J. K. Femtosecond Excited-State Dynamics of an Iron(II) Polypyridyl Solar Cell Sensitizer Model. *J. Am. Chem. Soc.* **2000**, *122*, 4092–4097.

(8) Juban, E. A.; Smeigh, A. L.; Monat, J. E.; McCusker, J. K. Ultrafast Dynamics of Ligand-Field Excited States. *Coord. Chem. Rev.* **2006**, *250*, 1783–1791.

(9) Wolf, M. M. N.; Groß, R.; Schumann, C.; Wolny, J. A.; Schünemann, V.; Døssing, A.; Paulsen, H.; McGarvey, J. J.; Diller, R. Sub-Picosecond Time Resolved Infrared Spectroscopy of High-Spin State Formation in Fe(II) Spin Crossover Complexes. *Phys. Chem. Chem. Phys.* **2008**, *10*, 4264–4273.

(10) Gawelda, W.; Cannizzo, A.; Pham, V.-T.; van Mourik, F.; Bressler, C.; Chergui, M. Ultrafast Nonadiabatic Dynamics of $[Fe^{II}(bpy)_3]^{2+}$ in Solution. *J. Am. Chem. Soc.* **2007**, *129*, 8199–8206.

(11) Hoselton, M. A.; Wilson, L. J.; Drago, R. S. Substituent Effects on the Spin Equilibrium Observed with Hexadentate Ligands on iron(II). *J. Am. Chem. Soc.* **1975**, *97*, 1722–1729.

(12) Kukura, P.; McCamant, D. W.; Mathies, R. A. Femtosecond Stimulated Raman Spectroscopy. *Annu. Rev. Phys. Chem.* **2007**, *58*, 461–488.

(13) Henry, W.; Coates, C. G.; Brady, C.; Ronayne, K. L.; Matousek, P.; Towrie, M.; Botchway, S. W.; Parker, A. W.; Vos, J. G.; Browne, W. R.; et al. The Early Picosecond Photophysics of Ru(II) Polypyridyl Complexes: A Tale of Two Timescales. *J. Phys. Chem. A* **2008**, *112*, 4537–4544.

(14) Maçôas, E. M. S.; Kananavicius, R.; Myllyperkiö, P.; Pettersson, M.; Kunttu, H. Relaxation Dynamics of $Cr(acac)_3$ Probed by Ultrafast Infrared Spectroscopy. *J. Am. Chem. Soc.* **2007**, *129*, 8934–8935.

(15) Juban, E. A.; McCusker, J. K. Ultrafast Dynamics of 2E State Formation in $Cr(acac)_3$. *J. Am. Chem. Soc.* **2005**, *127*, 6857–6865.

Chapter 4

Chromophore Dynamics in the PYP Photocycle from Femtosecond Stimulated Raman Spectroscopy

Reproduced with permission from "Chromophore Dynamics in the PYP Photocycle from Femtosecond Stimulated Raman Spectroscopy" by Mark Creelman, Masato Kumauchi, Wouter D. Hoff, and Richard A. Mathies. Submitted to the Journal of Physical Chemistry B, November 2013.

4.1 Abstract

Femtosecond stimulated Raman spectroscopy (FSRS) is used to examine the structural dynamics of the *para*-hydroxycinnamic acid (HCA) chromophore during the first 300 ps of the photoactive yellow protein (PYP) photocycle, as the system transitions from its vertically excited state to the early ground state *cis* intermediate, I_0. A downshift in both the C_7=C_8 and C_1=O stretches upon photoexcitation reveals that the chromophore has shifted to an increasingly quinonic form in the excited state, indicating a charge shift from the phenolate moiety toward the C_9=O carbonyl, which continues to increase for 170 fs. In addition, there is a downshift in the C_9=O carbonyl out of plane vibration on an 800 fs timescale as PYP transitions from its excited state to I_0 indicating that weakening of the hydrogen bond with Cys69 and out of plane rotation of the C_9=O carbonyl are key steps leading to photoproduct formation. HOOP intensity increases on a 3 ps timescale during the formation of I_0 signifying distortion about the C_7=C_8 bond. Once on the I_0 surface, the C_7=C_8 and C_1=O stretches blue shift, indicating recovery of charge to the phenolate, while persistent intensity in the HOOP and carbonyl out of plane modes reveal HCA to be a cissoid structure with significant distortion about the C_7=C_8 bond and of C_9=O out of the molecular plane.

4.2 Introduction

Photoactive yellow protein (PYP) is a small (125 residue 14 kDa) water-soluble, protein isolated from the purple halophilic bacterium *Halorhodospira halophila,* where it serves as the photoreceptor for blue light avoidance. PYP owes its yellow color to a deprotonated *para*-hydroxy-cinnamic acid chromophore (HCA) covalently bound to Cys69 via a thioester linkage and noncovalently secured by extensive hydrogen bonding interactions (**Figure 4.1**). Absorption of blue light (λ_{max} = 446 nm) by the HCA chromophore initiates the PYP photocycle, which involves *trans*-*cis* isomerization about the C_7=C_8 bond within a few ps, protonation of the chromophore on the μs timescale, followed by partial unfolding of the protein and the exposure of the chromophore binding pocket in a few ms. The PYP_{dark} structure and protonation state are reformed in several hundred ms.[1–3]

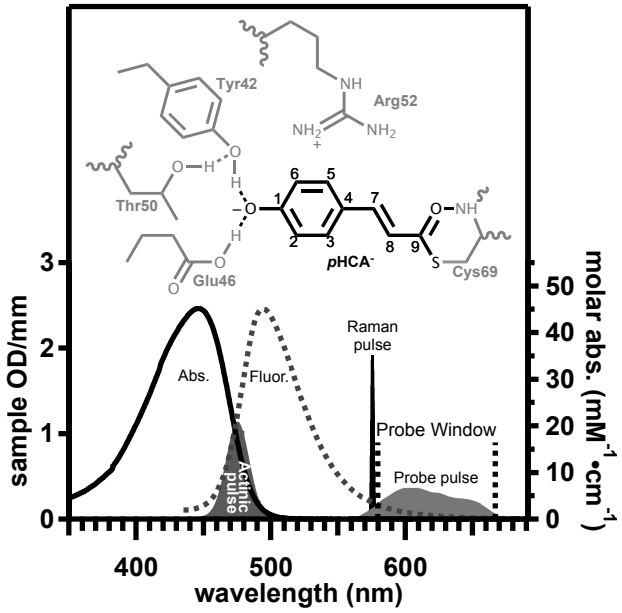

Figure 4.1 Structure of the *trans-p*-hydroxy-cinnamic acid PYP chromophore in the PYP_{dark} binding pocket. Optical parameters of the FSRS experiment are indicated over the PYP absorption (solid line, λ_{max} = 446 nm, ε_{446} = 45500 $M^{-1}cm^{-1}$) and fluorescence spectra (dotted line, λ_{max} = 495 nm). The actinic pulse, which initiates the PYP photocycle, was tuned to 475 nm. The 575 nm Raman and 577 - 667 nm Probe pulses lie in the red tail of the fluorescence band, and produce stimulated Raman spectra from 150-2200 cm^{-1}.

The primary photochemistry of the PYP photocycle, from the initial excitation through the formation of the early *cis*-isomerized photointermediates, has been studied using a variety of ultrafast techniques on native PYP as well as PYP mutants and analogs. Fluorescence up-conversion established that the excited state of PYP (pG*) decays multiexponentially with time constants of ~ 700 fs, ~ 3-10 ps and > 100 ps, with the two fastest decay components ascribed to twisting of the chromophore about its vinyl bond.[4,5] Femtosecond IR studies on the early PYP photocycle show that charge translocation from the phenolate towards the ethylenic tail of HCA occurs in the pG* state along with the weakening of the H bond between the HCA phenolate and Glu46.[6–8] UV ps Raman spectra of PYP also revealed changes in the hydrogen bonding between HCA and nearby protein residues, corroborating the weakening of the bond to Glu46 and showing that the H bond to Tyr42 is strengthened in the pG* state.[9] The Yoshizawa group published corroborating femtosecond Raman data from 800 to 1700 cm^{-1} where these shifts in the hydrogen bonding network were observed as early as 150 fs.[10] Recently, 8 fs pump-probe spectroscopy on the blue edge of the PYP absorption has revealed excited and ground state wave packets which suggest HCA adopts an increasingly quinonic form in its excited state, further supporting an excited state charge shift from the phenolate towards the ethylenic tail.[11] Femtosecond transient absorption (TA),[12–14] pump-probe IR[6,7] spectroscopies and ultrafast transient absorption anisotropy measurements[15] have revealed the 3 ps formation of an early *cis*-isomerized, red-shifted (λ_{max} ~ 510 nm) ground-state intermediate, I_0. Thus, the early stages of the photocycle involve a rapid change in the excited state hydrogen bonding network preceding the quenching of the excited state of the chromophore through a twisting motion, followed by the emergence of the isomerized ground state photoproduct species.

Pump-dump-probe experiments have been used to characterize the connectivity of excited and ground state intermediates and to explore the multi-exponential decay processes that take place during the PYP photocycle. The data from these experiments can be interpreted through an inhomogeneous model or a homogeneous model. In the inhomogeneous model, structural inhomogeneity in the ground state leads to the population of several distinct excited states upon photo-excitation, each with a unique photoproduct yield. In the homogeneous model the excited state population has a time-dependent yield and evolves on a complex, multidimensional potential energy surface with quenching pathways that compete with the photocycle.[16,17] These studies have also revealed the presence of a ground state intermediate (GSI) which results from unsuccessful attempts at photocycle initiation and leads back to the PYP_{dark} state. In addition a multi-photon ionization pathway has been discovered which produces an ionized chromophore and solvated electron.[8,18]

The proposed mechanism for the ultrafast *trans-cis* isomerization of the HCA chromophore is through the out of plane rotation of the thioester linkage between HCA and the protein. This mechanism is essentially required as a result of the discovery by Xie et al.[19] that the phenolate moiety is held in place by hydrogen bonds during the isomerization.[7,19–21] At the thioester end of the HCA chromophore, the C_9=O carbonyl is hydrogen bonded to the protein backbone of Cys69, while the phenolate end of HCA is held in place by hydrogen bonds between C_1-O^- and Tyr42, Glu46 and Thr50 (**Figure 4.1**).[20] While the hydrogen bonds to the phenolate oxygen are conserved during the initial *trans-cis* isomerization, the hydrogen bond between the C_9=O carbonyl and Cys69 is broken in this process.[6–8,20,21] These observations have lead to the conclusion that the carbonyl group rotates out of the plane of the chromophore while the phenolate moiety remains static during the early stages of C_7=C_8 photoisomerization.

To learn more about the chromophore structure and dynamics during the primary stages of the PYP photocycle we turn to femtosecond stimulated Raman Spectroscopy (FSRS)[22]. The FSRS technique has been invaluable in studying the structural dynamics of photochemical processes including charge transfer[23,24] and ultrafast isomerizations occurring in protein systems,[25–28] owing to its high structural (~ 20 cm^{-1}) and temporal (~ 50 fs) resolution, along with its ability to selectively enhance scattering from specific chromophore groups. High time resolution allows FSRS to track the structural details of non-stationary states in ultrafast photoreactions.[28] Structural changes along the reaction coordinate are revealed through frequency shifts observed in the time-resolved FSRS spectra. Finally, it is advantageous to implement the FSRS technique because TA and vibrational spectra are simultaneously acquired, allowing for direct association between structural dynamics and electronic transitions.

The FSRS study presented here provides high-quality time-resolved structural data over the first 300 ps following PYP photoexcitation, including the pG*, I_0 and I_1 intermediates. By extending the probed window down to 350 cm^{-1}, and following the reaction for several hundred ps with improved time resolution we are able to present a detailed analysis of structurally important, low-frequency modes, in addition to correlating the FSRS data with simultaneously collected transient absorption spectra. This work reveals the ultrafast dynamics of the C_1=O, C_9=O, and C_7=C_8 bond strengths and out of plane distortion on the initially formed excited state and in the transition from the excited state to the photoproduct ground state providing a clearer picture of the mechanism of photoactivation in PYP.

4.3 Experimental Methods

PYP was prepared as described previously[29–31] and in Appendix B. Briefly apo-PYP of *Halorhodospira halophila* was expressed in *E. coli* and extracted with 8 M urea. Holo-PYP was reconstituted in 4 M urea by the addition of *p*-coumaric anhydride. The PYP was purified using column chromatography (DEAE-sepharose) and concentrated for analysis with ultrafiltration membranes. For FSRS experiments, the protein was concentrated to 0.75 OD/mm at 475 nm in a 10 mM Tris buffer (pH 7.0, 5% glycerol). This sample was circulated through a 1 mm pathlength optical flow cell (Starna, 48-Q-1). Sample integrity was confirmed with UV-vis before and after experiments.

The FSRS instrument has been described in detail elsewhere.[22,32] In brief, a 1 kHz regenerative Ti:sapphire amplifier (Spectra-Physics, Spitfire, ~900 μJ pulses at 800 nm) with a duration of ~ 150 fs is used to generate the three pulses necessary for FSRS, which are presented along with the absorption and fluorescence spectra of PYP in **Figure 4.1**. The actinic pulse (475 nm, 890 cm^{-1}, 30 fs, 300 nJ/pulse) was generated using a home-built non-collinear optical parametric amplifier (NOPA).[33] The Raman pulse (575 nm, 25 cm^{-1}, ~ 590 fs, 300 nJ/pulse) was produced using a home-built narrow band OPA.[34] The continuum probe pulse (577-677 nm, ~ 30 nJ/pulse) was generated by focusing a small portion of the fundamental into a sapphire plate. This continuum was compressed in a BK7 prism pair and used to stimulate the Stokes Raman transitions. All powers quoted are measured at the sample. The 90 fs temporal instrument response was measured using the optical Kerr effect between the actinic and probe pulses in the sample buffer and cell (**Figure B.1**).[35] The actinic pulse duration was determined by measuring the autocorrelation signal in 0.2 mm BBO. The Raman pulse bandwidth and duration were determined from the line widths of the cyclohexane Raman signals (assuming a transform limited pulse). Cyclohexane was also used as the standard for Raman shift calibration. The three pulses are non-collinearly focused onto the sample using a 100 mm focal length achromatic lens. After passing through the sample, actinic and Raman pulses are blocked by an aperture, while the probe pulse is re-collimated with a 100 mm lens and focused into a spectrograph (Spex, 500M, 600 gr/mm, 500 nm blaze) and dispersed onto a front-illuminated CCD (Princeton Instruments, Pixis 100F). The CCD is synchronized to the 1 kHz amplifier pulse train so that each pulse can be read out separately. Phase-locked chopping of the Raman pulse at 500 Hz, and the actinic pulse at 250 Hz, allows for collection of the dark-state and photo-excited FSRS spectra as well as transient absorption in the probe window for a given delay time in 4 laser shots (4 ms) (**Figure B.2**).[24]

Time-resolved FSRS spectra were collected by varying the time delay between the actinic pulse and the Raman/probe pulse pair using a computer controlled delay stage (Physik Instrumente, M-405). The displayed spectra are averages of several thousand laser shots. The general data analysis procedure is presented in **Figure B.3**. The PYP_{dark} FSRS spectrum is produced by subtracting a scaled buffer spectrum and a small baseline from the raw dark state FSRS spectrum. To produce the time-resolved FSRS spectra of photoexcited PYP, each timepoint is corrected for transient Raman pump effects, solvent and PYP_{dark} contributions, as well as other transient effects such as electronic absorption and emission. Stimulated emission adds to the number of Raman pump photons, which is observed as a transient increase in the FSRS signal. To correct for this, each photoexcited timepoint is normalized by comparing the intensity of the 1641 cm^{-1} OH bending mode of water with the non-photoexcited spectrum. The

PYP_{dark} and buffer signals are then subtracted from each normalized timepoint. This step removes the contribution from the buffer but results in negative features due to over-subtraction of the dark state signals. This over-subtraction, which is due to the depleted population of PYP_{dark} after photoexcitation, is corrected by the addition of a scaled, buffer-subtracted, PYP_{dark} spectrum to each timepoint. The scale factor used in the depletion correction is related to the recovery of the PYP_{dark} species after photoexcitation (**Figure B.4**). A broad featured baseline is then subtracted from each timepoint to highlight the transient Raman bands of the photo-excited species. Kinetic analysis is performed by fitting FSRS peaks to Gaussian line shapes. The time evolution of the resulting frequencies and amplitudes are then fit to exponential functions convoluted with the 90 fs instrument response function.

4.4 Results

Transient absorption (TA) data on PYP collected in the 578 to 665 nm probe window are presented in **Figure 4.2**. The top panel (A) displays selected wavelength resolved spectra of photoexcited PYP, from 200 fs to 300 ps. At early times (< 1 ps) the ΔA spectra exhibit a large stimulated emission feature attributed to pG* at wavelengths shorter than ~645 nm and a small positive feature assigned to solvated electron generation due to photoionization at longer wavelengths. Though it has been previously reported that the photoionization pathway is inaccessible with 470 nm actinic pulses,[16] the assignment was confirmed by the observation of a quadratic dependence of the red absorption on the power of the actinic pulse. The strong stimulated emission (SE) feature from pG* decays rapidly, leaving a small emission signal at wavelengths shorter than 595 nm after 5 ps. By 20 ps all of the SE has decayed and the ΔA is small and positive over the entire probe window. The absorption feature, observed for wavelengths greater than 645 nm at early times, increases for the first several ps. After ~ 5 ps the absorption signal begins decaying and continues to diminish for the duration of the experiment as the solvated electron and radical chromophore recombine.

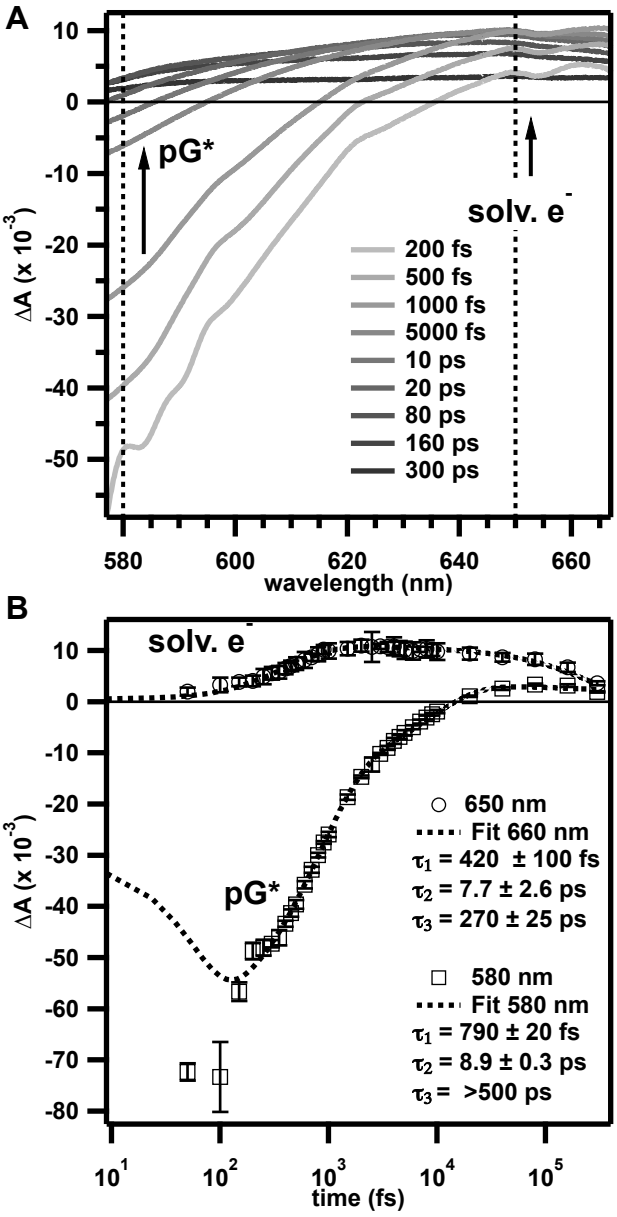

Figure 4.2 Transient absorption of PYP in the 577-677 nm probe window. (A) Selected transient absorption difference spectra from -2000 to 300 ps. (B) Kinetic data and fits for 580 nm (squares) and 650 nm (circles). Time constants for the fits are noted in the bottom panel.

Kinetic analysis of the TA features of pG* and the solvated electron are plotted as a function of time on a log scale in **Figure 4.2B**. The 580 nm SE feature due to pG* decays with a time constant $\tau_1 = 790 \pm 20$ fs, eventually transitioning into an absorption signal ($\tau_2 = 8900 \pm 300$ fs) after ~ 20 ps. This 580 nm absorption feature decays slowly, but not entirely ($\tau_3 > 500$ ps) through 300 ps, the longest delay time recorded. The solvated electron absorption feature at 650 nm initially grows in with a time constant of 420 ± 100 fs and reaches a maximum at ~ 2 ps, after which the signal decays on the multi-picosecond timescale ($\tau_2 = 7.7 \pm 2.6$ ps, $\tau_3 = 270 \pm 25$ ps). At 300 ps the ΔA spectrum remains slightly positive over the entire probe window. While the

time constants of the transient absorption are unaffected by the presence of the Raman pump, the amplitudes of the early decay and rise of the SE at 580 nm and the TA at 650 nm, respectively, are diminished, indicative of dumping of the excited pG* population by the Raman pump. The amplitude of the fast decay of the SE signal at 580 nm is decreased by 20% and the fast rise in the solvated electron TA at 650 nm decreases by nearly 60% in the presence of the Raman pump (**Figure B.5**).

The FSRS spectrum of PYP_{dark} presented at the bottom of **Figure 4.3** corresponds well with previously published resonance Raman spectra of the *p*-hydroxy-cinnamic acid chromophore.[21,36–38] However, due to the ~ 25 cm^{-1} bandwidth of the Raman pulse, close lying features are not resolved in the FSRS spectra. The following mode descriptions are based on the assignments of Unno et al.[38] and described here according to their major character. The intense ethylenic mode at 1555 cm^{-1} is assigned to C_7=C_8 stretching coupled with the phenolate stretch analogous to the Y19a mode of tyrosine, while the shoulder at 1639 cm^{-1} is assigned to C_9=O stretching. The bands at 1285, 1443, and 1510 cm^{-1} are all attributed to various CC vibrations of the aromatic ring; the 1285 and 1510 cm^{-1} modes are also coupled to the C_7=C_8 stretch. The 1160 cm^{-1} mode is the hydrogen in-plane bending vibration of the ring CH bonds. The 1049 cm^{-1} mode is assigned to the C_8-C_9 stretch. The C_7H=C_8H and ring C-H hydrogen out of plane (HOOP) wagging vibrations are observed at 979 cm^{-1}. The 894 cm^{-1} band is assigned to bending of the carbon chain ($C_7C_8C_9$). The 828 cm^{-1} band is assigned to CC ring torsion and stretching. The 754 cm^{-1} mode is primarily due to the C_9=O in plane bend coupled with ring CC and C_1-O stretching. The mode observed at 644 cm^{-1} is primarily due to the C_9=O carbonyl out-of-plane vibration. The peaks at 453 and 538 cm^{-1} are attributed to in-plane vibrations and deformations of the ring and $C_7C_8C_9$ tail.

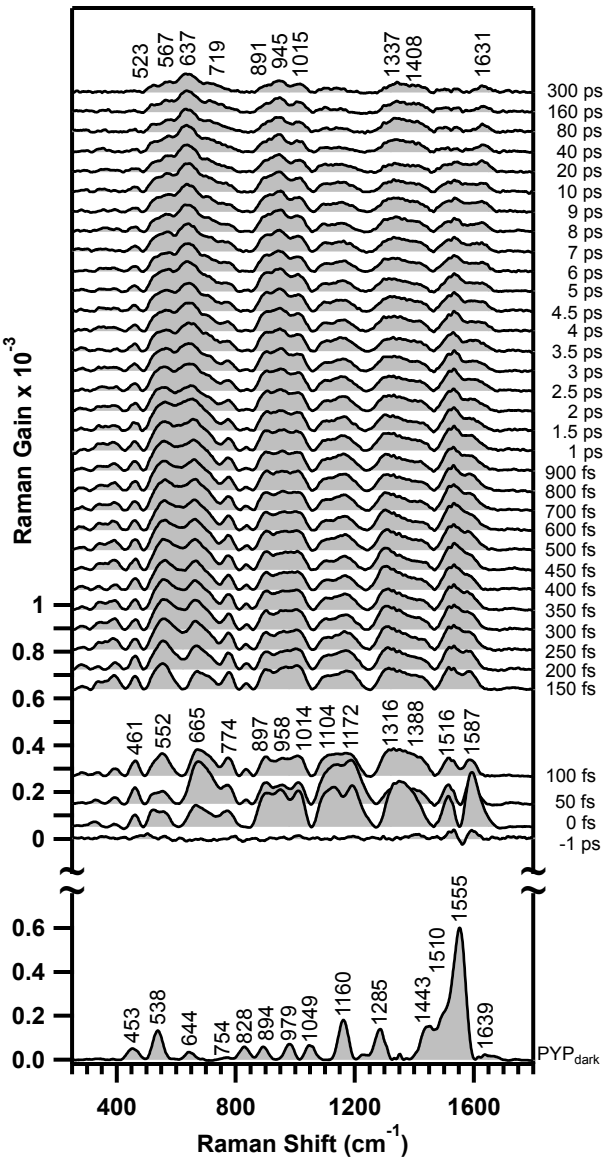

Figure 4.3 FSRS spectra of the *p*-hydroxy-cinnamic acid chromophore in PYP. The PYP_{dark} FSRS spectrum is displayed at the bottom. The time-resolved data from 0 fs to 300 ps are displayed above PYP_{dark} for comparison.

The structural dynamics of the first 300 ps of the PYP photocycle are presented as a stacked plot of the time-resolved FSRS spectra in **Figure 4.3**. Raman data of photoexcited PYP in the 800-1700 cm^{-1} spectral region are generally consistent with FSRS the data obtained during the first ps of the photocycle presented by Nakamura et al.[10] though intensities differ slightly. Upon photoexcitation, a vibrational spectrum featuring several moderate intensity bands from 900 to 1600 cm^{-1}, and a set of somewhat weaker bands between 400 and 800 cm^{-1} appears. These new features are readily observable after excitation, as their magnitudes are close to those observed for PYP_{dark}. Use of a 575 nm Raman pump pulse resulted in stokes FSRS spectra with negligible dispersion at early times, consistent with the findings of Nakamura et al. For the first 50 fs after excitation the observed intensities fluctuate. These fluctuations may arise from rapid

evolution on the excited state surface, however, they may also be due to artifacts created by the actinic pump, which is still impinging on the sample during this time. By 100 fs a spectral pattern that smoothly evolves through 300 ps is apparent. Linearity of the power-dependence of transient Raman signals has been confirmed, indicating they arise from photocycle intermediates arising from a single-photon pathway. Further, the 350 nm absorption of the radical, photoionized PYP[16] would gain little enhancement from the 575 nm Raman pulse, and is not expected to scatter strongly under the experimental conditions.

Because stimulated emission is observed during the first 10 ps after photoexcitation, Raman features observed during this time may be assigned partially to the decaying excited state, and will naturally contain the largest excited state contribution immediately following photoexcitation. The frequencies observed at early times are labeled in the 100 fs spectrum. Tentative assignments of these modes are made based on their proximity to dark state vibrational frequencies, and described according to their major contributing characters.[38] The peaks at 1516 and 1587 cm^{-1} fall in the region assigned to the C_7=C_8 stretch coupled with vibrations of the phenolate ring. However, the blue shift of the 1587 cm^{-1} shoulder to 1631 cm^{-1} by 300 ps suggest that this peak is likely associated with the C_9=O stretch that downshifts from 1639 cm^{-1} in PYP_{dark}.[21] The peaks at 1316 and 1388 cm^{-1} appear in a region relatively unpopulated by dark state signals. The 1316 cm^{-1} mode is assigned to hydrogen in plane wagging on HC_7=C_8H, which occurs at 1325 cm^{-1} in PYP_{dark}.[38] Based on its relatively large intensity the 1388 cm^{-1} peak may be due to hydrogen in plane bending and C-C stretching on the phenolate ring, which are seen at 1443 cm^{-1} in PYP_{dark}. However, the C_1-O stretch has been calculated[38] to fall between 1300 and 1400 cm^{-1} and increased intensity in this region may also be due to increased polarizability of this bond following photoexcitation. The peaks at 1104 and 1172 cm^{-1} are likely due to hydrogen in plane rocking vibrations, though the 1104 cm^{-1} peak may also correspond with an upshifted C_8-C_9 stretch. The peak at 1014 cm^{-1} is tentatively assigned to in-plane deformation of the phenolate ring, although this peak also lies very close to the region assigned to various hydrogen out of plane (HOOP) modes. The peak at 958 cm^{-1} is assigned to HOOP vibrations of the C_7=C_8 moiety. Skeletal vibrations and modes of the ethylenic tail of the chromophore are found below 900 cm^{-1}. Also found in this region is the C_9=O carbonyl out of plane vibration at 665 cm^{-1}.

Several trends are noticeable in the transient PYP spectra during the first picosecond following excitation. Many of the peaks continue to grow in from 200 - 500 fs after excitation, the most noticeable being those at 552, 665, 958 and 1516 cm^{-1}. After the first ~ 500 fs every peak is decaying except for the HOOP mode at 958 cm^{-1} which continues to gain intensity, and the 665 cm^{-1} C_9=O carbonyl out of plane mode which maintains much of its intensity. In addition to the intensities, the frequencies of certain bands are also evolving. The frequencies of the peaks at 1172, 958, and 665 cm^{-1} are all downshifting while the peak at 1516 cm^{-1} is upshifting during this time. The frequencies of both the 1316 and 1587 cm^{-1} bands also shift, but they downshift for the first ~ 500 fs followed by an increase in frequency.

The spectra evolve over the next several picoseconds as most of the intensities decay. By 40 ps the intensity of the 1516 cm^{-1} peak, as well as the signals observed between 1100 and 1200 cm^{-1} have grown very weak. From 40 to 300 ps the spectral pattern remains largely unchanged, save for a slight decrease in signal intensity. By 300 ps most of the remaining intensity is observed between 500 and 750 cm^{-1}, the region assigned to skeletal modes and

vibrations of the ethylenic tail. The next largest intensities are seen between 850 and 1050 cm^{-1} where HOOP vibrations are expected to occur. Intensity also remains at 1337 and 1408 cm^{-1}. A small peak is visible at 1631 cm^{-1}; this peak has blue shifted from the 1587 cm^{-1} shoulder observed at 100 fs and is assigned to the C_9-O stretch. Recovery to PYP_{dark}, determined from analysis of Raman depletion signals is presented in **Figure B.4.** The depletion decays multiexponentially with time constants of 50 ± 20 fs, 8.0 ± 0.8 ps and 900 ± 400 ps.

The amplitudes and frequencies for several key Raman bands are plotted as a function of time in **Figure 4.4**. The kinetics of these peaks, as well as those not featured in the figure, were fit to a multiexponential decay convoluted with the 90 fs instrument response. The kinetics were fit to a simple, linear model in order to highlight the time ordering of photocycle structural dynamics while remaining agnostic to the various connectivity schemes proposed for the PYP photocycle. Though the observed kinetics are complex, involving many bands evolving with several different time constants, global analysis of the data revealed that all of the FSRS kinetics are well fit using the following set of time constants: 170 ± 20 fs, 870 ± 90 fs, 2600 ± 150 fs, 14 ± 6.5 ps, 45 ± 9.6 ps and ~ 800 ps.

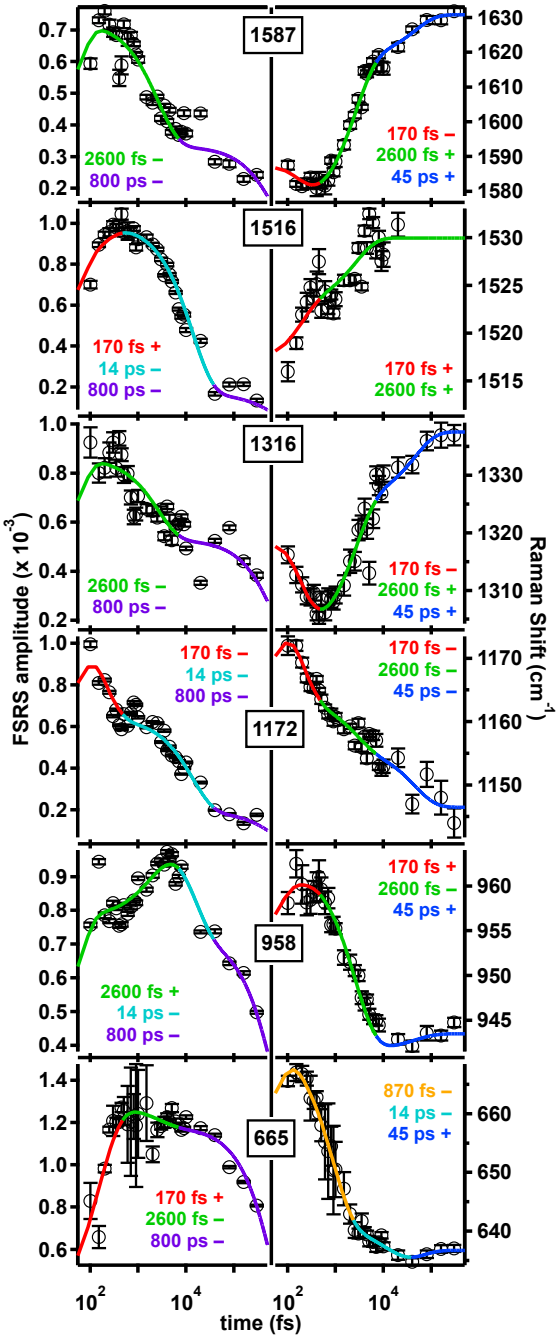

Figure 4.4 Kinetics of selected FSRS peaks. Time-resolved FSRS peaks were fit to Gaussian line shapes, and the resulting frequencies and amplitudes are plotted as a function of time above. The amplitudes are displayed in the left column while the frequencies are displayed on the right. Peaks are labeled by their 100 fs frequency. The data have been fit to multiexponential functions convoluted with the 90 fs instrument response function. The kinetics are well fit using the following set of time constants: 170 ± 20 fs, 870 ± 90 fs, 2600 ± 150 fs, 14 ± 6.5 ps, 45 ± 9.6 ps, and ~ 800 ps. Peaks are labeled with the relevant time constants. Rises and decays are indicated by + and - signs, respectively. The best-fit lines are color coded to indicate which time constant is describing the convoluted exponential function at a given time.

Looking at the amplitudes (**Figure 4.4**, left column) many different sets of dynamics are observed. The peaks at 1587 and 1316 cm^{-1} both decay with a 2600 fs time constant assigned to I_0 formation, followed by an ~ 800 ps decay. The ~ 800 ps decay component is shared by all of the FSRS amplitudes and is assigned to the loss of Raman enhancement as I_0 eventually decays to I_1, which absorbs maximally at 465 nm.[13] The peaks at 1516 and 1172 cm^{-1} also share a set of time constants, 170 fs, 14 ps and ~ 800 ps. While the 170 fs component corresponds to a growth at 1516 cm^{-1}, it corresponds to a decay at 1172 cm^{-1}. Because the 170 fs process occurs faster than the stimulated emission decay, it is assigned to excited state dynamics. The 14 ps process occurs on the same timescale as dark state recovery. The peaks at 958 and 665 cm^{-1} each undergo unique amplitude kinetics. The 665 cm^{-1} peak initially grows in on the excited state, with a time constant of 170 fs, after which it decays with the 2600 fs I_0 formation, and continues decaying during the transition to I_1. The 170 fs process is not observed for the peak at 958 cm^{-1}, which grows in with the 2600 fs I_0 formation, then decays with a 14 ps and an ~ 800 ps time constant.

The frequency kinetics are more homogeneous, with most kinetics fitting to the three time constants: 170 fs, 2600 fs and 45 ps. Shifts on these timescales reveal structural dynamics on the excited state, as well as those occurring during and following I_0 formation. The kinetics for the peak at 1516 cm^{-1} do not include the 45 ps component, as this peak has virtually disappeared after 20 ps. The frequency of the peak at 665 cm^{-1} was found to shift with different kinetics than the other peaks, and is best fit using the time constants 870 fs, 14 ps and 45 ps. The downshift of the 665 cm^{-1} peak could not be satisfactorily fit without the 870 fs component. These unique kinetics correspond well with the stimulated emission decay.

4.5 Discussion

Previous studies, employing time-resolved absorption,[12–14] fluorescence,[4,5,39] Raman[37,40] and IR[6–8] techniques have revealed a basic picture of the primary photochemistry of PYP. The FSRS data presented in this paper affirm these previous studies and also offer new information on the structural dynamics during the transition from pG* to the early photoproduct I_0, particularly through the 200-800 cm^{-1} data. In order to visualize the key changes associated with the kinetic processes identified above, FSRS spectra corresponding with each kinetic intermediate are presented in **Figure 4.5**.

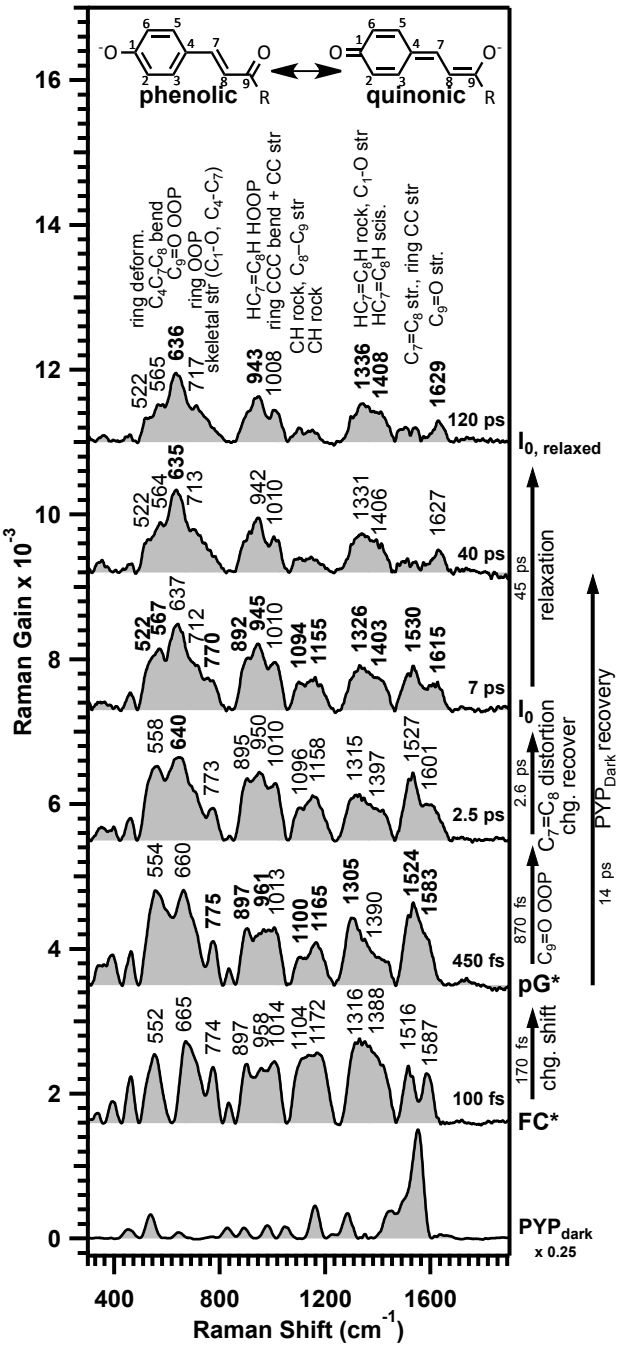

Figure 4.5 The FSRS spectra of observed kinetic intermediates. The 1/e time constant and the structural changes associated with each intermediate are indicated to the right of the spectra. The 120 ps spectrum is the average of the 80 and 160 ps timepoints, all other spectra correspond with the timepoints displayed in **Figure 4.3**. Bolded labels indicate which frequencies have shifted concurrently with the formation of each intermediate. Mode character assignments are listed above the corresponding peaks.

The FSRS spectra immediately following photoexcitation are strikingly different from the PYP_{dark} spectrum, featuring shifted frequencies and vastly different relative intensities. The early 100 fs species has been designated as the Franck-Condon excited state (FC*). Notably, peaks in the 400 - 700 cm^{-1} region have gained intensity at the expense the large ring modes at ~ 1550 cm^{-1}. The large relative intensities throughout the spectrum are indicative of broken symmetry. In particular, the HOOP intensity at 958 cm^{-1} is characteristic of distortion about the C_7=C_8 double bond. Large changes in both the dipole moment and polarizability of the photoexcited HCA chromophore have been previously observed using Stark-effect spectroscopy, indicating a charge shift in the excited state.[41] Redistribution of the negative charge from the phenolate oxygen of HCA to the carbonyl would be expected to enhance the polarizability, and hence the Raman intensities of modes localized on the ethylenic tail with the opposite being true for modes of the phenolate ring. This charge redistribution is also expected to alter certain frequencies as the structure becomes increasingly quinonic.[42] In the quinonic form the C_7=C_8 and C_9=O bond orders should decrease while the C_4–C_7, C_8-C_9 and C_1–O^- bond orders should increase. This prediction is confirmed in the FC* spectrum (**Figure 4.5**) where the C_7=C_8 stretching dominated mode has downshifted to 1516 cm^{-1} and the C_9=O stretch has downshifted to 1587 cm^{-1}. The new peak at 1104 cm^{-1} could correspond with an upshifted C_8-C_9 stretch. The C_1-O stretch is very weak and not resolved in our PYP_{dark} spectrum, but has previously been observed at 1343 cm^{-1}.[38] New intensity at 1390 cm^{-1} in the FC* spectrum may correspond to an upshifted C_1-O stretch, which would be expected to gain intensity with increasing double-bond character. The observed intensity and frequency changes in the 100 fs spectrum are consistent with a charge-shifted, distorted FC* state.

The FC* state then undergoes a transition with a time constant of 170 ± 20 fs that is significantly faster than the stimulated emission decay. This process is interpreted as excited state evolution from the initially formed FC* state to an increasingly charge shifted pG* as the chromophore nuclei respond to the instantaneous dipole change[41] induced by photoexcitation. During this transition it is likely that the deprotonated chromophore settles further into the quinonic form, increasing localization of the charge on the C_9=O oxygen.[42] Key structural changes occurring with pG* formation include a downshift of the C_9=O stretching frequency from 1587 to 1583 cm^{-1} consistent with the expected lowering of the C_9=O bond order in the quinonic form. The hydrogen in plane vibrations observed at 1172 cm^{-1} in the excited state, downshift to 1165 cm^{-1} which may result from decreasing the bond order of the C_7=C_8 stretch, but may also result from twisting of the H_7C=C_8H hydrogens out of the local plane. The frequency of the 1516 cm^{-1} mode also upshifts on this timescale to ~ 1524 cm^{-1}; the indicated increase in the C_7=C_8 bond order would be inconsistent with increasing quinonic form of the chromophore. However, this mode is coupled to the C_2=C_3 and C_5=C_6 stretches in the ring, which would both be expected to increase in bond order upon a phenolic to quinonic transition. These observations indicate that initial movements from the FC* state are driven by a charge relocation which may prime the system for isomerization by lowering the C_7=C_8 bond order. The 450 fs FSRS spectrum of the relaxed pG* state displayed in **Figure 4.5** represents the completion of this process.

Following the excited state charge shift, the C_9=O carbonyl out of plane vibration at 665 cm^{-1} downshifts to 640 cm^{-1} with a time constant of 870 ± 90 fs. It has been previously demonstrated, based on ultrafast IR studies, that a requirement for successful entry into the PYP photocycle is the breaking of the hydrogen bond between C_9=O and Cys69.[8] Breaking or

weakening of the hydrogen bond with Cys69 would be expected to reduce the restoring force, and thus lower the frequency of the C_9=O out of plane vibration, as observed, thus providing compelling support for this hypotheses. These kinetics closely match the previously observed 700 fs excited state decay[4,5,12,14] as well as the 790 fs stimulated emission decay reported here. The absence of a 700 fs decay component in studies on PYP assembled with locked chromophore analogues has lead to the assignment of this kinetic process to twisting of the *p*-hydroxy-cinnamic acid chromophore.[4,5] We suggest that this out-of-plane motion of C_9=O is the initial trajectory leading to the ground state surface and successful entrance into the photocycle. The spectrum resulting from the completion of this process is represented by the 2.5 ps timepoint displayed in **Figure 4.5**. This spectrum likely also contains contributions from longer-lived excited state and ground state species not leading to the photocycle.

After the downshift of the C_9=O carbonyl out of plane vibration, many frequencies and intensities evolve with a 2.6 ± 0.2 ps time constant, in good agreement with the reported kinetics for the formation of the *cis* photoproduct, I_0.[13,14] The C_9=O stretch upshifts from 1583 to 1615 cm^{-1}, consistent with a return of the charge towards its dark state phenolic configuration. The frequency of the C_7=C_8 stretch + ring mode at 1516 cm^{-1} continues to upshift on this timescale to 1530 cm^{-1}. A downshift in the hydrogen in plane region to 1155 cm^{-1} is likely due to further torsion along the C_7=C_8 bond, which relieves steric repulsions, allowing for lower frequency in plane motion. This conclusion is further supported by the increase in the HOOP intensities and their downshift to 943 cm^{-1} on this timescale indicating increased distortion of the C_7=C_8 bond and a twisted cisoid structure for I_0.

Following the formation of I_0, structural changes observed in the FSRS data are subtle, and are dominated by amplitude decay. A process occurring with a timescale of ~ 10 ps is observed in fluorescence decay, dark state recovery, and FSRS kinetics (8.9 ± 0.3, 8 ± 0.8 and 14 ± 6.5 ps, respectively). This process likely involves the return to the dark state from the previously identified GSI, whose lifetime has been reported as ~ 6 ps in addition to longer lived, unproductive excited state population that has also been reported to fall back in to the dark state.[8] This recovery occurs on the same timescale as a ~ 5 cm^{-1} downshift of the C_9=O carbonyl out of plane vibration from 640 to 635 cm^{-1}. Loss of Raman intensity from the GSI and excited state species as they return to the dark state configuration, leaving behind the cissoid, non-H-bonded photoproduct, may be expected to further reduce the overall observed frequency of the C_9=O carbonyl out of plane mode. The 40 ps spectrum in **Figure 4.5** results from the completion of this recovery process. If this interpretation is correct, timepoints prior to 40 ps will contain vibrational features of both the excited state, ground state photocycle intermediates and GSI leading back to the dark state, while timepoints following 40 ps will be due primarily to photocycle intermediates.

The dark state recovery kinetics in **Figure B.4** show that ~15% of the excited molecules recover directly to the dark state within the first few hundred fs. By 20 ps an additional 50% of dark state depletion has been filled in, leaving 35% of the initially excited population in the photocycle or photoionization pathway. Photoionization likely accounts for less than 5% of the photoexcited population due to the rather large absorptivity of the solvated electron.[43] A ~ 30% conversion efficiency from pG* to the ground state photoproducts is consistent with previous results.[12,44] In the first few ps we observe a 75% decrease in the fluorescence signal, with the remaining 25% decaying by 20 ps.

Finally, frequencies are observed to slightly upshift with a 45 ps ± 9.6 ps time constant. This process is assigned to relaxation of the chromophore and protein in the I_0 state. A spectrum of this species is displayed as $I_{0,\,relaxed}$ in **Figure 4.5**. The remaining HOOP intensity at 943 cm^{-1} indicates that $I_{0,\,relaxed}$ is still highly distorted about the C_7=C_8 bond. This stored distortion energy may be mechanistically important because it can be used to drive later structural changes in the photocycle. The 45 ps relaxation of I_0 is followed by an amplitude decay with a time constant of ~ 800 ps as I_0 decays to I_1.

Recently, Schotte et al. published time-resolved Laue structures of the PYP photocycle taken with only 150 ps resolution. Their earliest recorded photointermediate crystal structure, which nominally corresponds to the two longest FSRS timepoints measured in our experiment, shows a distorted cissoid structure with the C_9=O carbonyl displaced ~ 90º out of the phenolate plane but still hydrogen bonded with Cys69.[45] While photocycle intermediates trapped in a crystal don't necessarily directly correspond with those observed in solution, it is clear that this crystal structure geometry would involve a weaker hydrogen bond between C_9=O and Cys69. Thus both the Laue data and our observation of a reduced C_9=O out of plane vibrational frequency support a reduced hydrogen bond strength between C_9=O and Cys69 in $I_{0,relaxed}$.

4.6 Conclusions

In summary, we have observed the vibrational structural dynamics taking place during the early events of the PYP photocycle. This work provides new structural evidence for an excited state charge separation following the initial Franck Condon excitation. The decrease in the C_9=O stretching frequency within 200 fs indicates an increase in the charge localization on the carbonyl, which results from the molecule adopting an increasingly quinonic form. The C_9=O carbonyl out of plane vibration downshifts from 665 to 640 cm^{-1} concurrently with the fastest observed fluorescence decay component (τ ~ 800 fs), indicating that this motion lies along the reaction coordinate leading out of the excited pG* state and into the photocycle. This downshift in the carbonyl out of plane vibration results from the loss of restoring force as the hydrogen bond between C_9=O and Cys69 is weakened, and eventually broken. Once on the photoproduct surface, increases in the C_9=O and C_7=C_8 stretching frequencies indicate a restoration of the phenolic bond ordering, and thus the return of the negative charge to the phenolate moiety. The persistence of intensity in the HOOP region indicates that following relaxation I_0 remains highly distorted about the C_7=C_8 bond. Relieving this distortion is a likely driving force for the remaining PYP photocycle.

These new time-resolved structural data support an isomerization mechanism whereby the C_9=O carbonyl rotates out of plane, weakening its hydrogen bond with Cys69, and forming a distorted cissoid photoproduct intermediate, I_0 which likely stores energy used to further drive the photocycle. The data also provide insight into the role excited state charge shift plays in facilitating the carbonyl rotation, and thus, entrance into the PYP photocycle.

4.7 Acknowledgement

We thank Sangdeok Shim, for his laser expertise, David Hoffman, for his contributions to the instrument and data analysis tools, and Rosalie Tran and Jyotishman Dasgupta, for many helpful discussions. This work was supported by the Mathies Royalty Fund and NSF grant MCB-1051590 to W.D.H.

4.8 References

(1) Cusanovich, M. A.; Meyer, T. E. Photoactive Yellow Protein: A Prototypic PAS Domain Sensory Protein and Development of a Common Signaling Mechanism. *Biochemistry.* **2003**, *42*, 4759–4770.

(2) Hellingwerf, K. J.; Hendriks, J.; Gensch, T. Photoactive Yellow Protein, A New Type of Photoreceptor Protein: Will This "Yellow Lab" Bring Us Where We Want to Go? *J. Phys. Chem. A* **2003**, *107*, 1082–1094.

(3) Larsen, D. S.; van Grondelle, R. Initial Photoinduced Dynamics of the Photoactive Yellow Protein. *ChemPhysChem* **2005**, *6*, 828–837.

(4) Chosrowjan, H.; Mataga, N.; Nakashima, N.; Imamoto, Y.; Tokunaga, F. Femtosecond-Picosecond Fluorescence Studies on Excited State Dynamics of Photoactive Yellow Protein from Ectothiorhodospira Halophila. *Chem. Phys. Lett.* **1997**, *270*, 267–272.

(5) Changenet, P.; Zhang, H.; van der Meer, M. J.; Hellingwerf, K. J.; Glasbeek, M. Subpicosecond Fluorescence Upconversion Measurements of Primary Events in Yellow Proteins. *Chem. Phys. Lett.* **1998**, *282*, 276–282.

(6) Groot, M. L.; van Wilderen, L. J. G. W.; Larsen, D. S.; van der Horst, M. A.; van Stokkum, I. H. M.; Hellingwerf, K. J.; van Grondelle, R. Initial Steps of Signal Generation in Photoactive Yellow Protein Revealed with Femtosecond Mid-Infrared Spectroscopy. *Biochemistry.* **2003**, *42*, 10054–10059.

(7) Heyne, K.; Mohammed, O. F.; Usman, A.; Dreyer, J.; Nibbering, E. T. J.; Cusanovich, M. A. Structural Evolution of the Chromophore in the Primary Stages of Trans/Cis Isomerization in Photoactive Yellow Protein. *J. Am. Chem. Soc.* **2005**, *127*, 18100–18106.

(8) Van Wilderen, L. J. G. W.; van der Horst, M. A.; van Stokkum, I. H. M.; Hellingwerf, K. J.; van Grondelle, R.; Groot, M. L. Ultrafast Infrared Spectroscopy Reveals a Key Step for Successful Entry into the Photocycle for Photoactive Yellow Protein. *Proc. Natl. Acad. Sci. U. S. A.* **2006**, *103*, 15050–15055.

(9) Mizuno, M.; Kamikubo, H.; Kataoka, M.; Mizutani, Y. Changes in the Hydrogen-Bond Network around the Chromophore of Photoactive Yellow Protein in the Ground and Excited States. *J. Phys. Chem. B* **2011**, *115*, 9306–9310.

(10) Nakamura, R.; Hamada, N.; Abe, K.; Yoshizawa, M. Ultrafast Hydrogen-Bonding Dynamics in the Electronic Excited State of Photoactive Yellow Protein Revealed by Femtosecond Stimulated Raman Spectroscopy. *J. Phys. Chem. B* **2012**, *116*, 14768–14775.

(11) Liu, J.; Yabushita, A.; Taniguchi, S.; Chosrowjan, H.; Imamoto, Y.; Sueda, K.; Miyanaga, N.; Kobayashi, T. Ultrafast Time-Resolved Pump–Probe Spectroscopy of PYP by a Sub-8 fs Pulse Laser at 400 Nm. *J. Phys. Chem. B* **2013**, *117*, 4818–4826.

(12) Baltuska, A.; van Stokkum, I. H. M.; Kroon, A.; Monshouwer, R.; Hellingwerf, K. J.; van Grondelle, R. The Primary Events in the Photoactivation of Yellow Protein. *Chem. Phys. Lett.* **1997**, *270*, 263–266.

(13) Ujj, L.; Devanathan, S.; Meyer, T. E.; Cusanovich, M. A.; Tollin, G.; Atkinson, G. H. New Photocycle Intermediates in the Photoactive Yellow Protein from Ectothiorhodospira Halophila: Picosecond Transient Absorption Spectroscopy. *Biophys. J.* **1998**, *75*, 406–412.

(14) Devanathan, S.; Pacheco, A.; Ujj, L.; Cusanovich, M.; Tollin, G.; Lin, S.; Woodbury, N. Femtosecond Spectroscopic Observations of Initial Intermediates in the Photocycle of the Photoactive Yellow Protein from Ectothiorhodospira Halophila. *Biophys. J.* **1999**, *77*, 1017–1023.

(15) Gensch, T.; Gradinaru, C. C.; van Stokkum, I. H. M.; Hendriks, J.; Hellingwerf, K. J.; van Grondelle, R. The Primary Photoreaction of Photoactive Yellow Protein (PYP): Anisotropy Changes and Excitation Wavelength Dependence. *Chem. Phys. Lett.* **2002**, *356*, 347–354.
(16) Larsen, D. S.; Stokkum, I. H. M. van; Vengris, M.; Horst, M. A. van der; Weerd, F. L. de; Hellingwerf, K. J.; Grondelle, R. van. Incoherent Manipulation of the Photoactive Yellow Protein Photocycle with Dispersed Pump-Dump-Probe Spectroscopy. *Biophys. J.* **2004**, *87*, 1858–1872.
(17) Larsen, D. S.; van Grondelle, R.; Hellingwerf, K. J. Primary Photochemistry in the Photoactive Yellow Protein: The Prototype Xanthopsin. In *Ultrashort Laser Pulses in Biology and Medicine*; Biological And Medical Physics Biomedical Engineering; Springer Berlin Heidelberg, 2008; pp. 165–199.
(18) Zhu, J.; Paparelli, L.; Hospes, M.; Arents, J.; Kennis, J. T. M.; van Stokkum, I. H. M.; Hellingwerf, K. J.; Groot, M. L. Photoionization and Electron Radical Recombination Dynamics in Photoactive Yellow Protein Investigated by Ultrafast Spectroscopy in the Visible and Near-Infrared Spectral Region. *J. Phys. Chem. B* **2013**, *117*, 11042–11048.
(19) Xie, A.; Hoff, W. D.; Kroon, A. R.; Hellingwerf, K. J. Glu46 Donates a Proton to the 4-Hydroxycinnamate Anion Chromophore During the Photocycle of Photoactive Yellow Protein. *Biochemistry.* **1996**, *35*, 14671–14678.
(20) Genick, U. K.; Soltis, S. M.; Kuhn, P.; Canestrelli, I. L.; Getzoff, E. D. Structure at 0.85 Å Resolution of an Early Protein Photocycle Intermediate. *Nature* **1998**, *392*, 206–209.
(21) Unno, M.; Kumauchi, M.; Sasaki, J.; Tokunaga, F.; Yamauchi, S. Resonance Raman Spectroscopy and Quantum Chemical Calculations Reveal Structural Changes in the Active Site of Photoactive Yellow Protein. *Biochemistry.* **2002**, *41*, 5668–5674.
(22) Kukura, P.; McCamant, D. W.; Mathies, R. A. Femtosecond Stimulated Raman Spectroscopy. *Annu. Rev. Phys. Chem.* **2007**, *58*, 461–488.
(23) Brown, K. E.; Veldkamp, B. S.; Co, D. T.; Wasielewski, M. R. Vibrational Dynamics of a Perylene–Perylenediimide Donor–Acceptor Dyad Probed with Femtosecond Stimulated Raman Spectroscopy. *J. Phys. Chem. Lett.* **2012**, *3*, 2362–2366.
(24) Fujisawa, T.; Creelman, M.; Mathies, R. A. Structural Dynamics of a Noncovalent Charge Transfer Complex from Femtosecond Stimulated Raman Spectroscopy. *J. Phys. Chem. B* **2012**, *116*, 10453–10460.
(25) Kukura, P.; McCamant, D. W.; Yoon, S.; Wandschneider, D. B.; Mathies, R. A. Structural Observation of the Primary Isomerization in Vision with Femtosecond-Stimulated Raman. *Science* **2005**, *310*, 1006–1009.
(26) Shim, S.; Dasgupta, J.; Mathies, R. A. Femtosecond Time-Resolved Stimulated Raman Reveals the Birth of Bacteriorhodopsin's J and K Intermediates. *J. Am. Chem. Soc.* **2009**, *131*, 7592–7597.
(27) Dasgupta, J.; Frontiera, R. R.; Taylor, K. C.; Lagarias, J. C.; Mathies, R. A. Ultrafast Excited-State Isomerization in Phytochrome Revealed by Femtosecond Stimulated Raman Spectroscopy. *Proc. Natl. Acad. Sci. U. S. A.* **2009**, *106*, 1784–1789.
(28) Frontiera, R. R.; Fang, C.; Dasgupta, J.; Mathies, R. A. Probing Structural Evolution along Multidimensional Reaction Coordinates with Femtosecond Stimulated Raman Spectroscopy. *Phys. Chem. Chem. Phys.* **2011**, *14*, 405–414.

(29) Imamoto, Y.; Ito, T.; Kataoka, M.; Tokunaga, F. Reconstitution Photoactive Yellow Protein from Apoprotein and P-Coumaric Acid Derivatives. *FEBS Lett.* **1995**, *374*, 157–160.
(30) Mihara, K.; Hisatomi, O.; Imamoto, Y.; Kataoka, M.; Tokunaga, F. Functional Expression and Site-Directed Mutagenesis of Photoactive Yellow Protein. *J. Biochem.* **1997**, *121*, 876–880.
(31) Kumauchi, M.; Hamada, N.; Sasaki, J.; Tokunaga, F. A Role of Methionine100 in Facilitating PYPM-Decay Process in the Photocycle of Photoactive Yellow Protein. *J. Biochem.* **2002**, *132*, 205–210.
(32) Shim, S.; Mathies, R. A. Development of a Tunable Femtosecond Stimulated Raman Apparatus and Its Application to B-Carotene. *J. Phys. Chem. B* **2008**, *112*, 4826–4832.
(33) Wilhelm, T.; Piel, J.; Riedle, E. Sub-20-Fs Pulses Tunable Across the Visible from a Blue-Pumped Single-Pass Noncollinear Parametric Converter. *Opt. Lett.* **1997**, *22*, 1494–1496.
(34) Shim, S.; Mathies, R. A. Generation of Narrow-Bandwidth Picosecond Visible Pulses from Broadband Femtosecond Pulses for Femtosecond Stimulated Raman. *Appl. Phys. Lett.* **2006**, *89*, 121124.
(35) McCamant, D. W.; Kukura, P.; Yoon, S.; Mathies, R. A. Femtosecond Broadband Stimulated Raman Spectroscopy: Apparatus and Methods. *Rev. Sci. Instrum.* **2004**, *75*, 4971–4980.
(36) Kim, M.; Mathies, R. A.; Hoff, W. D.; Hellingwerf, K. J. Resonance Raman Evidence That the Thioester-Linked 4-Hydroxycinnamyl Chromophore of Photoactive Yellow Protein Is Deprotonated. *Biochemistry.* **1995**, *34*, 12669–12672.
(37) Pan, D.; Philip, A.; Hoff, W. D.; Mathies, R. A. Time-Resolved Resonance Raman Structural Studies of the pB' Intermediate in the Photocycle of Photoactive Yellow Protein. *Biophys. J.* **2004**, *86*, 2374–2382.
(38) Unno, M.; Kumauchi, M.; Tokunaga, F.; Yamauchi, S. Vibrational Assignment of the 4-Hydroxycinnamyl Chromophore in Photoactive Yellow Protein. *J. Phys. Chem. B* **2007**, *111*, 2719–2726.
(39) Chosrowjan, H.; Mataga, N.; Shibata, Y.; Imamoto, Y.; Tokunaga, F. Environmental Effects on the Femtosecond−Picosecond Fluorescence Dynamics of Photoactive Yellow Protein: Chromophores in Aqueous Solutions and in Protein Nanospaces Modified by Site-Directed Mutagenesis. *J. Phys. Chem. B* **1998**, *102*, 7695–7698.
(40) Mizuno, M.; Hamada, N.; Tokunaga, F.; Mizutani, Y. Picosecond Protein Response to the Chromophore Isomerization of Photoactive Yellow Protein: Selective Observation of Tyrosine and Tryptophan Residues by Time-Resolved Ultraviolet Resonance Raman Spectroscopy. *J. Phys. Chem. B* **2007**, *111*, 6293–6296.
(41) Premvardhan, L. L.; van der Horst, M. A.; Hellingwerf, K. J.; van Grondelle, R. Stark Spectroscopy on Photoactive Yellow Protein, E46Q, and a Nonisomerizing Derivative, Probes Photo-Induced Charge Motion. *Biophys. J.* **2003**, *84*, 3226–3239.
(42) Gromov, E. V.; Burghardt, I.; Hynes, J. T.; Köppel, H.; Cederbaum, L. S. Electronic Structure of the Photoactive Yellow Protein Chromophore: Ab Initio Study of the Low-Lying Excited Singlet States. *J. Photochem. Photobiol. Chem.* **2007**, *190*, 241–257.
(43) Jha, K. N.; Bolton, G. L.; Freeman, G. R. Temperature Shifts in the Optical Spectra of Solvated Electrons in Methanol and Ethanol. *J. Phys. Chem.* **1972**, *76*, 3876–3883.

(44) Van Brederode, M. E.; Gensch, T.; Hoff, W. D.; Hellingwerf, K. J.; Braslavsky, S. E. Photoinduced Volume Change and Energy Storage Associated with the Early Transformations of the Photoactive Yellow Protein from Ectothiorhodospira Halophila. *Biophys. J.* **1995**, *68*, 1101–1109.
(45) Schotte, F.; Cho, H. S.; Kaila, V. R. I.; Kamikubo, H.; Dashdorj, N.; Henry, E. R.; Graber, T. J.; Henning, R.; Wulff, M.; Hummer, G.; et al. Watching a Signaling Protein Function in Real Time via 100-Ps Time-Resolved Laue Crystallography. *Proc. Natl. Acad. Sci. U. S. A.* **2012**, *109*, 19256–19261.

Chapter 5

Conclusions and Prospects

5.1 Conclusions and Prospects

The time resolved Raman studies presented in this thesis establish femtosecond stimulated Raman spectroscopy (FSRS) as a versatile and powerful technique for studying ultrafast structural dynamics in both natural and synthetic photoreactive systems.

In Chapter 3 I present the structural dynamics of photoinduced spin-crossover in $[Fe(tren(py)_3)]^{2+}$ with sub-100 fs time resolution which has allowed for the unambiguous characterization of this process's timescale for the first time. The rapid structural evolution observed in this study has important implications for the use of iron(II) based materials as electron donors in dye sensitized solar cells (DSSCs) as well as magneto-optic devices. While the rapid spin-crossover process is promising for magneto-optical switching applications, it presents a significant obstacle for the use of iron based dyes in DSSCs as electron transfer from the quintet state is believed to be inefficient.[1]

In order to test the hypotheses formed on the basis of these results it will be necessary to perform a systematic study of compounds designed with the goal of learning if we can synthetically control the rate of intersystem crossing and quintet state formation. Because the formation of the quintet state is closely tied to the expansion of the ligand-sphere,[2,3] FSRS studies on iron(II) compounds with structures designed to limit ligand expansion would be useful in characterizing our ability to synthetically control this process. Once it is possible to control the rate of quintet state formation we can examine how this parameter controls efficiency. The development of simple design principles would be a massive advance in the field of DSCCs. In performing these studies it will be useful to apply tunable FSRS to $[Fe(tren(py)_3)]^{2+}$ and other similar systems in order to broaden the spectral window to include low frequency vibrations, and identify other potentially important structural dynamics, including the direct observation of metal-ligand vibrations. Furthermore, though the features of intermediate electronic states are expected to be quite broad due to their short lifetimes, the acquisition of data with improved time resolution, resonance enhancement, and the vastly improved signal to noise of shot-to-shot detection may reveal new information about the transition from the initially excited MLCT state to the ligand-field manifold that efficiently couples to the quintet state. Though their efficiency has remained stagnant for several years,[4] further development of non-ruthenium based DSSCs would increase the economic and environmental viability of the technology.

In Chapter 4 I present the structural dynamics of the photoactive yellow protein (PYP) chromophore directly showing that the C_9=O out of plane vibration is a key motion leading from the excited state to the isomerized early photocycle intermediates, the first direct structural observation confirming the carbonyl out of plane rotation mechanism for isomerization.

Additionally these studies reveal a charge shift in the excited state following excitation and recovery following the successful entry into the photocycle.

The successful application of FSRS to the PYP system, including the direct observation of the out-of-plane vibration, offers the opportunity to thoroughly explore protein-chromophore interactions. As the prototype structural model for the PAS signaling domain, as well as the xanthopsins[5,6] PYP serves as a well-characterized system on which to build a fundamental understanding of biological photoactivity. The structural dynamics of PYP engineered with modified chromophores would provide an excellent test of the conclusions presented in Chapter 4, as well as revealing other possible pathways that may potentially contribute to the photocycle. Of particular interest would be PYP generated with locked chromophore analogues that are unable to rotate the carbonyl group effectively.[7,8] Additionally, measuring the effects of the protein environment on the structural dynamics by mutating specific residues in the protein pocket would reveal precisely how the proteins functionally tune the photochemistry.[9] Though studies on PYP mutants exist, a thorough characterization of the relationship between these modifications and how they map to structural dynamics is lacking. Now that I have demonstrated the ability to track a key motion relevant to the isomerization mechanism with FSRS it will be possible to develop a clear picture of how the PYP's photochemistry is dictated by its structure.

5.2 References

(1) Monat, J. E.; McCusker, J. K. Femtosecond Excited-State Dynamics of an Iron(II) Polypyridyl Solar Cell Sensitizer Model. *J. Am. Chem. Soc.* **2000**, *122*, 4092–4097.

(2) Khalil, M.; Marcus, M. A.; Smeigh, A. L.; McCusker, J. K.; Chong, H. H. W.; Schoenlein, R. W. Picosecond X-Ray Absorption Spectroscopy of a Photoinduced Iron(II) Spin Crossover Reaction in Solution. *J. Phys. Chem. A* **2006**, *110*, 38–44.

(3) Bressler, C.; Milne, C.; Pham, V. T.; ElNahhas, A.; Veen, R. M. van der; Gawelda, W.; Johnson, S.; Beaud, P.; Grolimund, D.; Kaiser, M.; et al. Femtosecond XANES Study of the Light-Induced Spin Crossover Dynamics in an Iron(II) Complex. *Science* **2009**, *323*, 489–492.

(4) Hagfeldt, A.; Boschloo, G.; Sun, L.; Kloo, L.; Pettersson, H. Dye-Sensitized Solar Cells. *Chem. Rev.* **2010**, *110*, 6595–6663.

(5) Cusanovich, M. A.; Meyer, T. E. Photoactive Yellow Protein: A Prototypic PAS Domain Sensory Protein and Development of a Common Signaling Mechanism. *Biochemistry.* **2003**, *42*, 4759–4770.

(6) Larsen, D. S.; van Grondelle, R.; Hellingwerf, K. J. Primary Photochemistry in the Photoactive Yellow Protein: The Prototype Xanthopsin. In *Ultrashort Laser Pulses in Biology and Medicine*; Biological And Medical Physics Biomedical Engineering; Springer Berlin Heidelberg, **2008**; pp. 165–199.

(7) Changenet, P.; Zhang, H.; van der Meer, M. J.; Hellingwerf, K. J.; Glasbeek, M. Subpicosecond Fluorescence Upconversion Measurements of Primary Events in Yellow Proteins. *Chem. Phys. Lett.* **1998**, *282*, 276–282.

(8) Chosrowjan, H.; Taniguchi, S.; Mataga, N.; Unno, M.; Yamauchi, S.; Hamada, N.; Kumauchi, M.; Tokunaga, F. Low-Frequency Vibrations and Their Role in Ultrafast Photoisomerization Reaction Dynamics of Photoactive Yellow Protein. *J. Phys. Chem. B* **2004**, *108*, 2686–2698.

(9) Chosrowjan, H.; Mataga, N.; Shibata, Y.; Imamoto, Y.; Tokunaga, F. Environmental Effects on the Femtosecond−Picosecond Fluorescence Dynamics of Photoactive Yellow Protein: Chromophores in Aqueous Solutions and in Protein Nanospaces Modified by Site-Directed Mutagenesis. *J. Phys. Chem. B* **1998**, *102*, 7695–7698.

Appendix A

Experimental Procedures for Femtosecond Time-Resolved Optical and Raman Spectroscopy of Photoinduced Spin Crossover: Temporal Resolution of Low-to-High Spin Optical Switching

A.1 General

The syntheses of $[Fe(tren(py)_3)](PF_6)_2$ (Compound **1** in **Figure 3.1**) and $[Fe(tren(6\text{-}Me\text{-}py)_3)](PF_6)_2$ (Compound **2** in **Figure 3.1**) have been described previously.[1,2] The composition and purity of the samples were verified by elemental and mass spectral analyses carried out at the Analytical Facilities of Michigan State University. Steady-state electronic absorption spectra were collected on a Hewlett-Packard model 8452 UV/VIS spectrophotometer. Electrochemical and spectroelectrochemical data were acquired using a BAS-50W electrochemical analyzer employing a standard three-electrode set up (Pt working and counter-electrodes and a $Ag/AgNO_3$ reference). The spectroelectrochemical data are plotted in **Figure A.1**.

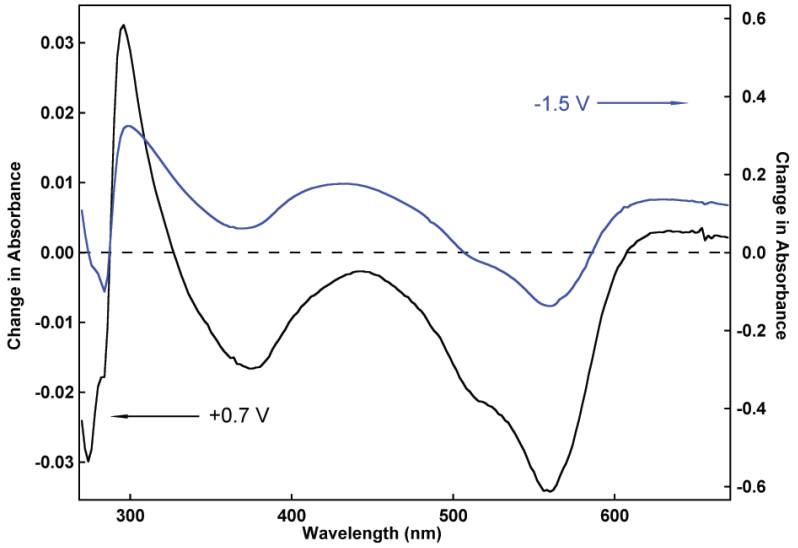

Figure A.1 Steady-state spectroelectrochemical data for $[Fe(tren(py)_3)](PF_6)_2$ in CH_3CN solution containing 0.1 M $(NBu_4)(PF_6)$. The data were acquired using a standard three-electrode set-up consisting of Pt working and counter-electrodes and a $Ag/AgNO_3$ reference. Both the reductive (blue) and oxidative (black) spectra are plotted as difference spectra using the ground-state absorption spectrum of $[Fe(tren(py)_3)](PF_6)_2$ as the baseline; the potentials at which the data were collected are indicated in the figure. The absorption spectrum of the initially formed charge-transfer state created following excitation in the visible can be approximated by a weighted linear combination of these two difference spectra.

A.2 Nanosecond Time-Resolved Transient Absorption Spectroscopy

Transient absorption data on $[Fe(tren(py)_3)](PF_6)_2$ were collected using a nanosecond time-resolved absorption spectrometer that has been previously described,[3] subject to the following modifications: probe wavelengths higher in energy of 350 nm required exchanging the glass achromats and cemented doublets, which composed the probe beam path, for quartz singlets. With the quartz lenses, probe wavelengths from 270 nm to approximately 900 nm were available. Samples were prepared with an optical density between 0.5 and 0.8 at the excitation wavelength of 560 nm. Excitation energies were on the order of 2 mJ at 560 nm and yielded a linear response from the sample with respect to pump power. Data at each wavelength comprise an average of 15 traces, with each trace corresponding to 15 pulses of laser light coincident with 15 flashes of probe light. Kinetics were well represented by a single exponential function; the excited-state lifetime of $\tau = 60 \pm 5$ ns was found to be independent of probe wavelength and consistent with previously published results.[1] The difference spectrum illustrated in **Figure 3.2** was generated by plotting the pre-exponential factor obtained from the fits obtained at each probe wavelength.

A.3 Femtosecond Time-Resolved Absorption Spectroscopy

The ultrafast pump-probe spectrometer used herein has been reported previously.[3] Samples of $[Fe(tren(py)_3)](PF_6)_2$ were dissolved in aerated CH_3CN at an optical density of ca. 0.6-0.8 (1 mm path length quartz cuvette) at the excitation wavelength of 560 nm: this wavelength corresponds to the peak of the lowest energy metal-to-ligand charge transfer (MLCT) absorption of the compound. Neat solvent or a two-photon absorber, such as trichlorotoluene in acetonitrile, was used to establish $\Delta t = 0$. The excitation energy was attenuated with neutral density filters and adjusted to a value that ensured a linear molecular response. Data were acquired using pump energies on the order of 5-6 μJ at 560 nm. Linearity of the signal with respect to pump power was verified for each sample. Electronic absorption spectra measured before and after data acquisition confirmed the integrity of the sample.

Depending on the probe wavelength of interest, single wavelength kinetic traces were acquired by selecting a small portion of the continuum with 10 nm band-pass filters as described previously[3] or by probing at the desired wavelength with the output from a second Light Conversions TOPAS. Single wavelength kinetic traces acquired at wavelengths higher in energy than 350 nm required the use of a second Light Conversions TOPAS (TOPAS 2). As described in reference 3, both TOPAS 1 and 2 are pumped with the 805 nm output from a Positive Light Spitfire Ti:sapphire regenerative amplifier (1 W, 85 fs). TOPAS 2, pumped with 0.2 mJ, 805 nm, provides wavelengths between 12 μm and 237 nm. Software designed and provided by Light Conversions provided facile control over the output wavelength from the TOPAS. All generation processes were controlled within the TOPAS system by the software; the harmonic processes employed for wavelength generation are specified here for clarity. UV probe wavelengths between 270 - 300 nm were obtained by sum frequency mixing of the second harmonic of the idler and the pump, while the fourth harmonic of the signal provided access to probe wavelengths between 290 - 400 nm. Dichroic wavelength separators, supplied by Light Conversions, were used to reflectively filter out lower energy harmonics of the probe beam while maintaining the temporal integrity of the pulse. The output from TOPAS 2 was linearly polarized either vertically or horizontally depending on the wavelength. Manipulation of the

probe beam was essential to ensure magic angle polarization was maintained with respect to the pump beam. The polarization of the TOPAS 2 output was therefore rotated by configuring two uncoated Al mirrors such that the polarization of the reflected beam was at 54° relative to the polarization of the pump; magic angle at the sample was verified by passing the probe beam through two sheets of polarizing film. The output from the TOPAS 2 was attenuated with quartz neutral density filters prior to the sample to ensure linear response of the signal (~5% of the pump energy) and passed through the appropriate 10 nm band pass filter prior to detection at the wavelengths of interest. A solution of trichlorotoluene (TCT) in acetonitrile was employed to measure the instrument response function (IRF) of the UV-probe/visible pump set-up. The cross correlation signal of the TCT at 290 nm probe with 560 nm pump was fit to a Gaussian function with a full-width-at-half-maximum (FWHM) of ~250 fs.

Fitting of UV transient absorption kinetic data was done using a locally generated procedure in WaveMetrics IGOR Pro, where the IRF of the system was fixed to the FWHM value obtained from fitting the cross correlation signal mentioned above. Data were fit via iterative reconvolution of the IRF (represented by a Gaussian line shape having a FWHM of 250 fs) convolved with an exponential kinetic model. Successful convergence was evaluated based on a visual inspection of the fit.

A.4 Femtosecond Stimulated Raman Spectroscopy

The apparatus and methods for FSRS have been previously detailed.[4] Briefly, a titanium:sapphire oscillator is used to produce 1 kHz, 50 fs, 800 μJ pulses at 792 nm. The narrow bandwidth, 2 ps Raman pump pulse (2.6 μJ) is produced by passing 85% of the amplifier output through a grating filter. The remaining amplifier output is used to generate the Raman probe and the actinic pump pulses. The probe is produced by passing a small portion of the amplifier output through a 3 mm sapphire plate, generating a white light continuum. This continuum passes through a 3 mm RG850 long-pass filter restricting it to wavelengths > 830nm, and is compressed to produce ~ 20 fs, 6 nJ IR continuum pulses. After compression the probe continuum is split to create a probe and reference. The actinic pump (400 nJ/pulse) is generated using non-collinear optical parametric amplification (NOPA), tuned to 560 nm, and compressed to 30 fs.[5,6] The probe beam is then collimated and focused into a spectrograph and dispersed onto a dual photodiode array detector. Data acquisition and actinic pump-Raman probe time delays are controlled by a LabVIEW program of local origin. The instrument response (90 ± 10 fs) was determined by cross-correlation between the actinic pump and Raman probe in the sample cell through the optical Kerr effect in acetonitrile. The spectra presented in Figure 3 result from an average of 2600 to 3000 accumulations using 60 ms exposures for an acquisition time of 156-180 s per time point.

Excited state FSRS spectra are obtained by first subtracting the ground state spectrum from the pumped spectra. Negative features due to depleted ground state population in the pumped spectra are then removed by adding a scaled fit of the ground state spectrum to each time point. These steps are illustrated in **Figure A.2**.

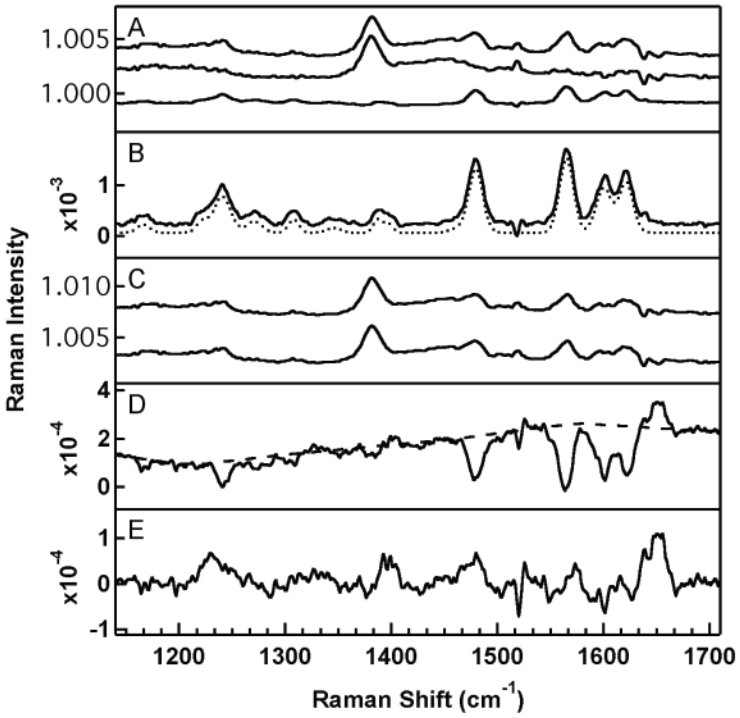

Figure A.2 The analysis of the FSRS data is illustrated above using the 5 ps time point. The ground state spectrum is generated by subtracting the acetonitrile-only spectrum (A, middle trace) from the sample spectrum (A, top trace), leaving only the features due to $[Fe(tren(py)_3)](PF_6)_2$ (A, bottom trace). The baseline is subtracted to generate the spectrum seen in panel B (solid line). The peaks in this spectrum are fit to Gaussian line shapes for analysis of the excited state spectra (B, dotted line). Excited state spectra are obtained by first subtracting the ground state spectrum (C, bottom trace) from the pumped spectrum (C, top trace) resulting in the spectrum in panel D. A baseline is subtracted (D, dashed line) and the depletion features are removed by adding in a scaled, fit ground state spectrum (B, dotted line) leaving only the excited state features (E).

For the FSRS experiments reported herein, crystalline $[Fe(tren(py)_3)](PF_6)_2$ was dissolved in acetonitrile to give an absorbance of ~2 at 558 nm in a 200 μm path length quartz flow cell, corresponding to a concentration of 6.05×10-5 M. UV-visible spectra taken before and after data acquisition showed no signs of photodegradation.

A.5 Steady-State Raman Spectra

The spontaneous Raman spectrum of $[Fe(tren(6\text{-}Me\text{-}py)_3)](PF_6)_2$ was obtained using the 676.4 nm line of a Kr+ laser at a concentration of 1.5×10^{-6} M and 11 mW of power. Scattered light was collected at 90º through a double monochromator (Spex 1401, 1200 grooves/mm) and imaged onto a CCD detector. The CCD response was corrected by dividing the spectra by a spectrum of white light produced by a tungsten filament bulb. The entrance slit was set to 200 μm, corresponding to a band pass of 4 cm^{-1}. Spectra were an average of 600 accumulations of 12 s exposures.

A.6 References

(1) Monat, J. E.; McCusker, J. K. Femtosecond Excited-State Dynamics of an Iron(II) Polypyridyl Solar Cell Sensitizer Model. *J. Am. Chem. Soc.* **2000**, *122*, 4092–4097.

(2) Hoselton, M. A.; Wilson, L. J.; Drago, R. S. Substituent Effects on the Spin Equilibrium Observed with Hexadentate Ligands on iron(II). *J. Am. Chem. Soc.* **1975**, *97*, 1722–1729.

(3) Juban, E. A.; McCusker, J. K. Ultrafast Dynamics of 2E State Formation in Cr(acac)3. *J. Am. Chem. Soc.* **2005**, *127*, 6857–6865.

(4) McCamant, D. W.; Kukura, P.; Yoon, S.; Mathies, R. A. Femtosecond Broadband Stimulated Raman Spectroscopy: Apparatus and Methods. *Rev. Sci. Instrum.* **2004**, *75*, 4971–4980.

(5) Cerullo, G.; De Silvestri, S. Ultrafast Optical Parametric Amplifiers. *Rev. Sci. Instrum.* **2003**, *74*, 1.

(6) Fork, R. L.; Martinez, O. E.; Gordon, J. P. Negative Dispersion Using Pairs of Prisms. *Opt. Lett.* **1984**, *9*, 150.

Appendix B

Supporting Information for Chromophore Dynamics in the PYP Photocycle from Femtosecond Stimulated Raman Spectroscopy

B.1 PYP Preparation

The PYP gene from *Halorhodospira halophila BN9626* was cloned into the pQE-80L plasmid (QIAGEN) between BamHI and HindIII sites to attach a 6-histidine tag and enterokinase cleavable site to the N-terminal side of the target protein. The plasmid for protein expression was transformed into *E. coli* BL21 (DE3, Stratagene). The cells were cultured at 37 °C in LB medium containing 50 mg/mL ampicilin overnight. Expression of *apo*-PYP was induced by the addition of isopropyl-thio-*β*-galactoside (IPTG; final concentration 1 mM) after 16–18 hr. After extra incubation for 4 hr, the cells were harvested by centrifugation at 4000 pm for 10 min (Sorvall Evolution® RC, SLC-6000 angle rotor). The harvested *E. coli* pellet was disrupted with 8 M urea (pH 8.0), and the cell debris removed by ultracentrifugation at 25,000 rpm for 20 min (Beckman Coulter, Optima™ L-90K Ultracentrifuge, Type-70Ti angle rotor).[1,2] The extracted water-soluble fraction was diluted with 20 mM Tris/Cl pH 7.5 until the urea concentration was 4 M, followed by the addition of *p*-coumaric anhydride as described.[3] The solution turned yellow with continuous stirring for 30 min at 4°C. The reconstituted crude PYP was dialyzed with buffer to remove the urea, and applied to Ni-NTA resin (QIAGEN). The column was washed with buffer, 5 mM imidazol and eluted with 200 mM imidazol. The Ni-NTA purified PYP was further purified with a DEAE-Sepharose CL6B column (GE Healthcare). After the column was washed with buffer, PYP was eluted with 100 mM NaCl in the same buffer. This process was repeated three times, and the purity was checked by UV-visible absorption spectrum until the ratio of A278nm/A446nm was < 0.45. PYP was then concentrated with an ultrafiltration membrane (Centriprep 10, Amicon) and diluted with buffer for use. Dilution and concentration steps were repeated several times to remove NaCl.[2]

B.2 Experimental Details

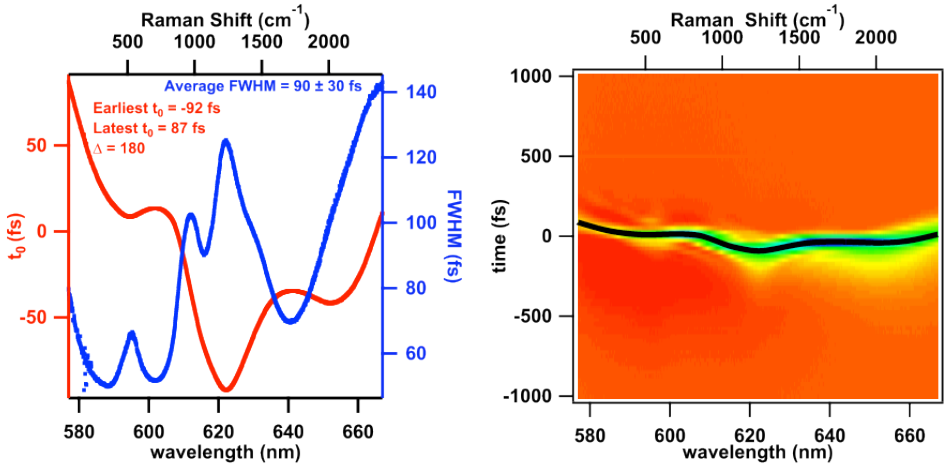

Figure B.1 Cross correlation measured using the optical Kerr effect. The graph on the left shows t = 0, the maximum of the Kerr signal (red), and the FWHM of the Kerr signal (blue) as a function of wavelength. The 2D plot at the right shows the measured Kerr signal from -1 ps to 1 ps as a function of wavelength, with t = 0 marked in black.

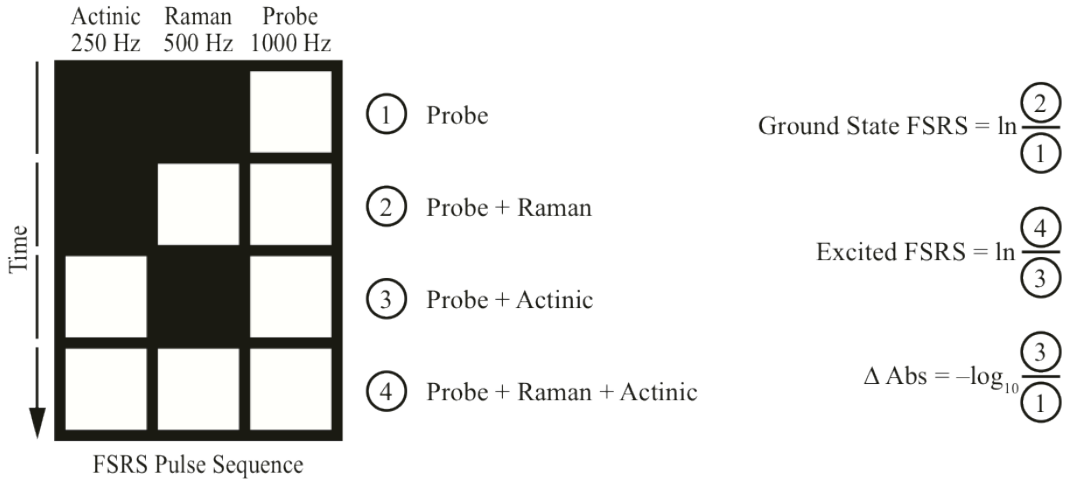

Figure B.2 Pulse-timing used for FSRS data acquisition. In the pulse sequence diagram (left) the pulse labels appear across the top with their respective chopping frequencies. White boxes denote the presence of a pulse, while black indicates blocking by an optical chopper. The detector is synced to the 1kHz pulse train of the amplifier, and reads out the dispersed probe signal shot by shot. By modulating the Raman and Actinic pulses as illustrated above, it is possible to collect ground state FSRS, excited state FSRS, and transient absorption spectra for a given time delay in 4 laser shots (4 ms). The general equations for producing FSRS gain and transient absorption spectra from the collected signals are shown at right.

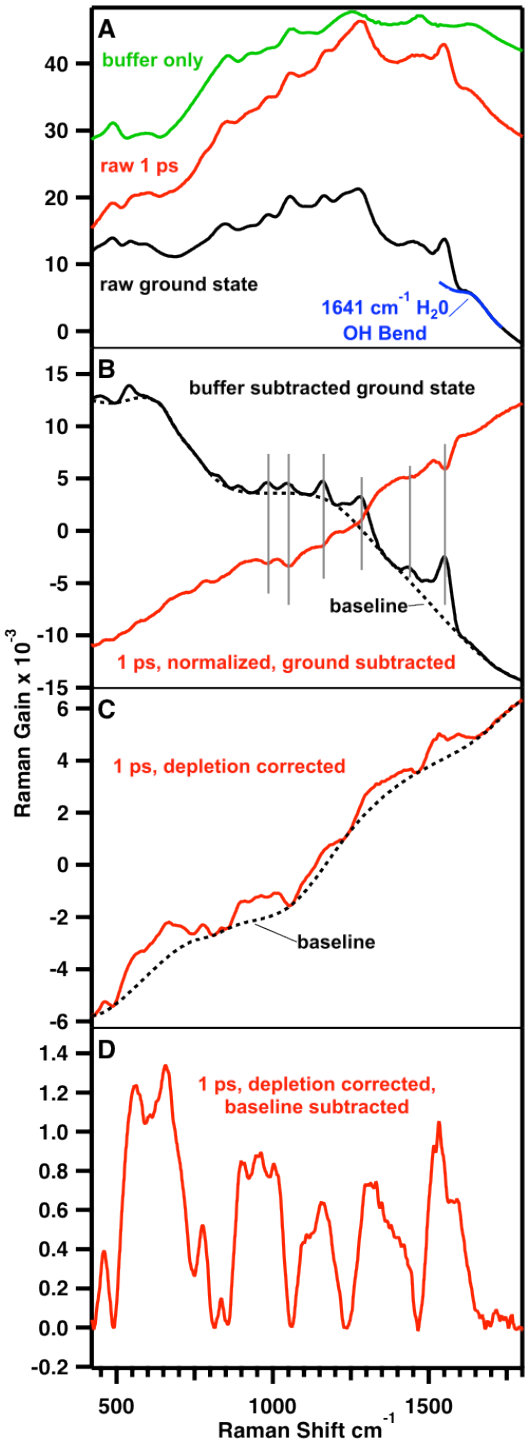

Figure B.3 General steps for FSRS data analysis. The process begins in panel A. In each of the steps (A-D) processing of the ground state FSRS spectrum is shown in black while processing of the excited FSRS spectrum (using the 1 ps timepoint as an example) is shown in red. Panel A shows the raw FSRS spectra for the ground state (A, black), the 1 ps time-point (A, red) and buffer only (A, green). The ground state signals of PYP are revealed by subtracting a scaled buffer-only spectrum (A, green) from the raw ground state spectrum (A, black). Contributions

from the ground state and buffer are removed from the excited spectra by first normalizing each timepoint to the raw ground state spectrum using the intensity of the 1641 cm^{-1} OH bend of water (A, blue) and then subtracting the raw ground state (A, black) from each normalized time-point. Panel B shows the buffer subtracted ground state data (B, black) along with the normalized 1 ps data after subtraction of the raw ground state signals (B, red). The 1 ps spectrum now contains features of the photo-excited species along with negative features arising from ground state depletion (marked with vertical grey lines). The depletion is removed by adding a scaled, buffer-subtracted ground state spectrum (B, black) to each timepoint. Panel C shows the result of the ground state depletion correction for the 1 ps timepoint (C, red). The remaining baseline (C, dotted black) is subtracted to produce the excited FSRS spectrum seen in Panel D (D, red).

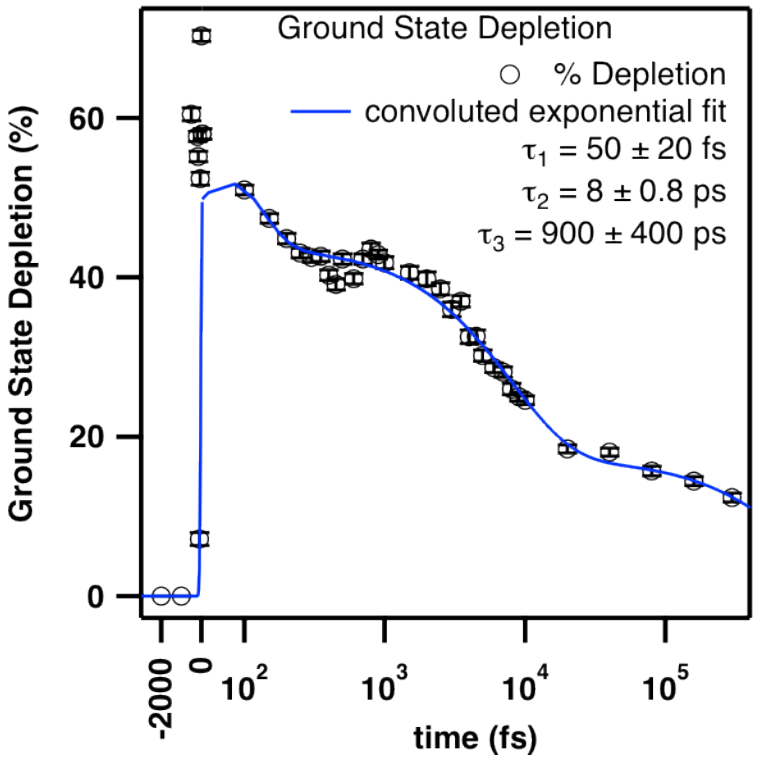

Figure B.4 Kinetic plot of ground state depletion as a function of log time. Following photoexcitation the population of PYP in the ground state decreases, reducing the signal due to ground state PYP in these spectra. When subtracting the raw ground state FSRS spectrum (which is necessary to remove peaks from the non-photoactive buffer) from excited timepoints results in over-subtraction features at the ground state frequencies. These are removed by adding a scaled ground-state-PYP-only spectrum (Figure S3, panel B, black) back to each normalized, subtracted timepoint (Figure S3, panel B, red). The amount of depletion reports on the recovery of the ground state species. The ground state depletion was fit to a convoluted exponential decay with three time constants; 50 fs, 8 ps, and 900 ps.

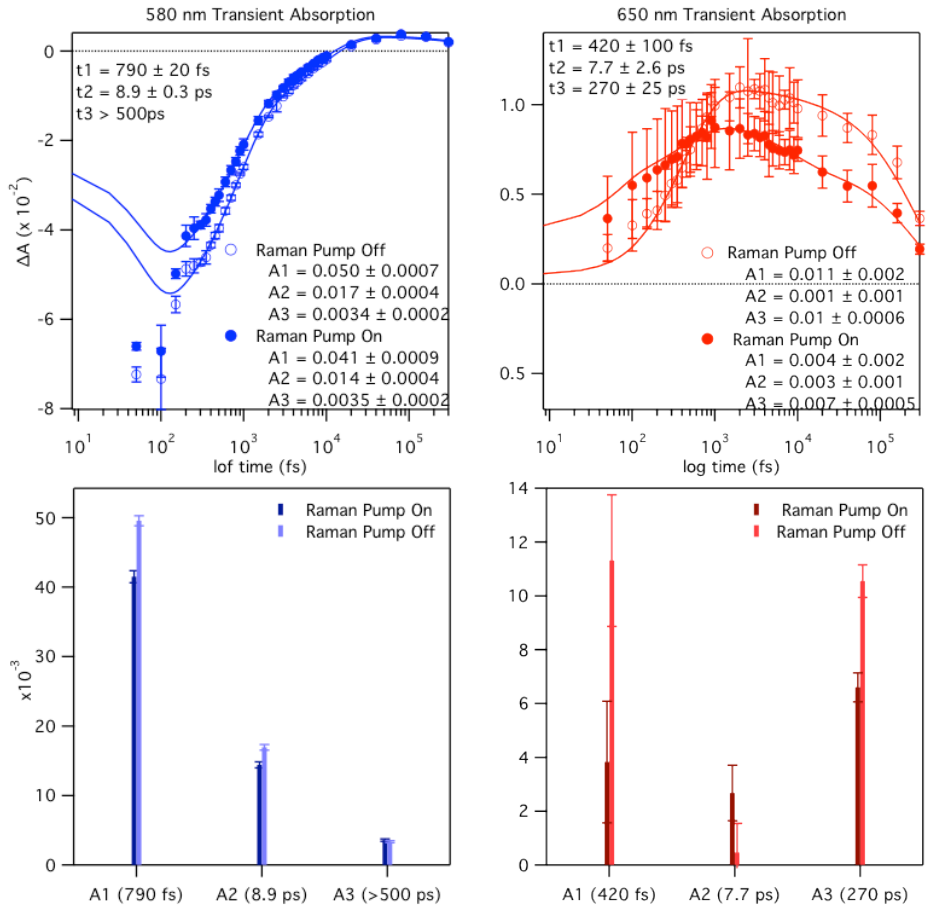

Figure B.5 Effects of Raman pump on transient absorption. The top panels show the transient absorption kinetic traces for 580 nm (blue) and 650 nm (red) recorded in the absence (open circles) and in the presence (closed circles) of the Raman pump pulse. The bottom panels compare the amplitudes of the exponential components when the Raman pump is on and off. The most pronounced effects are seen on the amplitude of the 420 fs rise of the absorption signal at 650 nm, which is nearly halved in the presence of the Raman pump.

B.3 References

(1) Mihara, K.; Hisatomi, O.; Imamoto, Y.; Kataoka, M.; Tokunaga, F. Functional Expression and Site-Directed Mutagenesis of Photoactive Yellow Protein. *J. Biochem.* **1997**, *121*, 876–880.

(2) Kumauchi, M.; Hamada, N.; Sasaki, J.; Tokunaga, F. A Role of Methionine100 in Facilitating PYPM-Decay Process in the Photocycle of Photoactive Yellow Protein. *J. Biochem.* **2002**, *132*, 205–210.

(3) Imamoto, Y.; Ito, T.; Kataoka, M.; Tokunaga, F. Reconstitution Photoactive Yellow Protein from Apoprotein and P-Coumaric Acid Derivatives. *FEBS Lett.* **1995**, *374*, 157–160.